STUDY ON MOLECULAR PHOTOIONIZATION IN FEMTOSECOND LASER FIELD

by

HUI LI

B. S., Nankai University, China, 2007
M. S., Nankai University, China, 2010

A THESIS

submitted in partial fulfillment of the requirements for the degree

MASTER OF SCIENCE

Department of Physics
College of Arts and Sciences

KANSAS STATE UNIVERSITY
Manhattan, Kansas

2013

Approved by:

Major Professor
Matthias Kling

Copyright

Abstract

This thesis consists of two major parts. The first part concerns studies of the orientation dependence of the ionization of diatomic molecules in intense, femtosecond two-color laser fields. The second part is about studies on the ionization mechanisms of the C_{60} molecule in femtosecond near-infrared and ultraviolet laser fields.

In the first part, experimental and theoretical results on the asymmetric ion emission of the heteronuclear molecules CO and NO in two-color laser fields are discussed. The two-color fields, which can be tailored by a relative phase, are used to ionize and dissociate CO and NO molecules, both of which are molecules with small polarizabilities. The resulting C^+, C^{2+}, N^+ and O^+ ions are detected by a velocity map imaging (VMI) setup. The photoelectrons from above-threshold ionization (ATI) of Xe are studied under such a two-color field to assign the phase. For both CO and NO we find that enhanced ionization occurs when the molecule is oriented with the electric field pointing from the C or N atom toward the O atom. This is in agreement with the molecular orbital Ammosov-Delone-Krainov (MO-ADK) theory and the Stark-corrected strong-field-approximation (SFA) calculations.

The second part is devoted to the investigation of the ionization mechanism of neutral C_{60} molecules with 30 fs laser pulses at about 800 nm and with 50 fs pulses at about 400 nm. The angular distributions of photoelectrons are measured utilizing VMI. Measurements under different intensities are carried out for the two wavelengths. In our work, thermal electron emission is highly suppressed by the use of short pulses. For near-infrared excitation, photoelectron angular distributions (PADs) that contain six lobes are observed for low energy electrons. This behavior is different from studies for longer pulses of about 120 fs [1]. Further analysis indicates that the PADs might originate from single photon ionization of a super atomic molecular orbital (SAMO), however, a detailed assignment requires further theoretical work. The PADs for the ultraviolet excitation show very similar structures to earlier results [1]. For the near-infrared excitation, we have carried out studies as a function of the chirp of the pulses and find effects on photoelectron spectra and on PADs, which are tentatively explained by sequential multiphoton ionization via “doorway” states.

Table of Contents

List of Figures

List of Tables

Acknowledgements

The most gratitude is given to my advisors, Prof. Matthias Kling and Prof. Lew Cocke. I do not know how to express my great appreciations to them. I want to thank my major advisor Matthias for his great help on every aspect during my master years. He taught me how to become a better physicist. I am very grateful to Lew who guided me for my first year in Kansas. He shared a lot of experiences on research and on life. He is so energetic and active that influences everyone around.

It was a great experience to work with all the nice people in JRML. Thanks to Sankar De who gave me the first impressions on the VMI setup and taught me a lot of valuable skills for research. Thanks to Zhenhua Wang who offers the most experimental supports during my master career. I appreciated the valuable discussions with Prof. Itzik Ben-Itzhak and Prof. Artem Rudenko. I would like to thank the other group members, Wei Cao, Guillaume Laurent, Yubarag Malakar, and Aram vajdi. I would like to thank Mohammad Zohrabi for a lot of valuable discussions and sharing optics. I would like to appreciate Kun Zhao, Baozhen Zhao, Xiaoming Ren, Kelsie Betsch and Charles Fehrenbach, who help to maintain the laser systems. A lot of theory support for this thesis is from Prof. Chii-Dong Lin's group: Anh-Thu Le and Wei-Chun Chu, without whom the work could not be nicely accomplished. There are also nice experiences cooperating with Prof. Vinod Kumarappan's group. I want to thank Prof. Uwe Thumm for his excellent lectures on quantum mechanics. This lecture is quite tough for most of the students, but we learned a lot.

I would like to thank all the technical support staff in JRML, including Mike Wells, Al Rankin, Scott Chainey, Bob Krause and Vince Needham. I want to give my gratitude especially to Al and Mike who help to design and build our VMI system and the C_{60} source, and they have been extremely supportive and helpful throughout my work.

I would like to appreciate all the department personnel: Peggy Matthews, Jane Peterson, Deanna Selby, Lindsay Thompson, and Kim Elliott. Your great efforts make the life in Physics department much easier and happier.

Furthermore, I want to give thanks to all the great friends that I met in KSU. There are a lot of nice guys around who lift me up in these years. I am so lucky to meet you here and I will cherish our friendship forever.

Last but not least, I want to thank my family for their great support on my study and research work, especially my parents and my husband who sacrifice a lot in their lives but help to make my dream come true. My dear daughter Wendy, without you this thesis might be accomplished much earlier, however, nothing can replace the happiness that you bring to my life. You are the most precious gift that I have ever got.

Dedication

This thesis is dedicated to my husband Zhenhua Wang and my daughter Wendy Wang, for the greatest love and happiness that they bring to my life.

Chapter 1 - Introduction

With the advent of ultrashort, femtosecond laser systems, the control and tracing of dynamical processes in atoms and molecules became feasible and has even progressed into the attosecond time domain [1-6]. Among all the light matter interaction processes, atomic and molecular photoionization processes are of great interest and have been studied for several decades [7-10]. Still, significant research is needed to fully understand light-matter interaction in the strong-field regime. In this thesis, we focus on investigations of the ionization characteristics both for diatomic molecules and for larger fullerene molecules in femtosecond laser fields.

1.1 Photoionization in strong femtosecond laser fields

When atoms or molecules are interacting with laser fields of sufficient intensity, photoionization will occur. Depending on the laser intensity being used, different ionization mechanisms are found [11]. As is shown in Fig. 1.1 (a) to (c), when a moderate laser intensity is used (10^{10} W/cm^2 to 10^{13} W/cm^2, for a typical rare gas atom with an ionization potential between 12 eV and 24 eV), multiphoton processes are usually dominating photoionization. If the electron is directly ionized to the continuum by more than one photon, as shown in Fig. 1.1(a), it is called multiphoton ionization (MPI) [8, 12]. It was observed that the *n*-photon ionization rate was proportional to I^n, where I is the laser intensity, n is the number of photons. If there exists a resonant energy level as shown in Fig. 1.1(b), ionization rate will be enhanced by the resonance and result in resonant enhanced multiphoton ionization (REMPI) [13, 14]. When the laser intensity is sufficiently high ($I > 10^{11}$ W/cm^2), photons in excess numbers can be absorbed. There will be several peaks appearing in the photoelectron spectrum, separated by one photon energy. This corresponds to above threshold ionization (ATI) [15, 16], which is shown in Fig. 1.1(c). The position of the ATI peaks is predictable by

$$E=(n+s)\hbar\omega-I_{p.} \qquad (1.1)$$

Here, E is the electron kinetic energy, n is the number of photons needed to overcome the ionization potential, s is the number of excess photons, which can be 0, 1, 2, 3, etc., ω is the angular frequency of the laser field, and I_p is the ionization potential.

For sub-picosecond pulses, an AC Stark shift may occur, which can be estimated by the ponderomotive energy U_p. The ATI spectrum becomes more complicated [15], and the corresponding electron kinetic energy $\tilde{E}$ will be

$$\tilde{E}=(n+s)\hbar\omega-(I_p+U_p). \qquad (1.2)$$

Here, U_p is the ponderomotive energy, which is defined as the kinetic energy of an electron quivering in the laser field, averaged over an optical cycle. In a linearly polarized monochromatic laser field, the non-relativistic expression for the U_p is

$$U_p = \frac{e^2 E_0^2}{4m\omega^2}. \qquad (1.3)$$

Here, e is the electron charge, E_0 is the amplitude of the electric field, and m is the electron mass. In atomic units (a.u.), U_p equals $\frac{I}{4\omega^2}$, where I denotes the laser peak intensity.

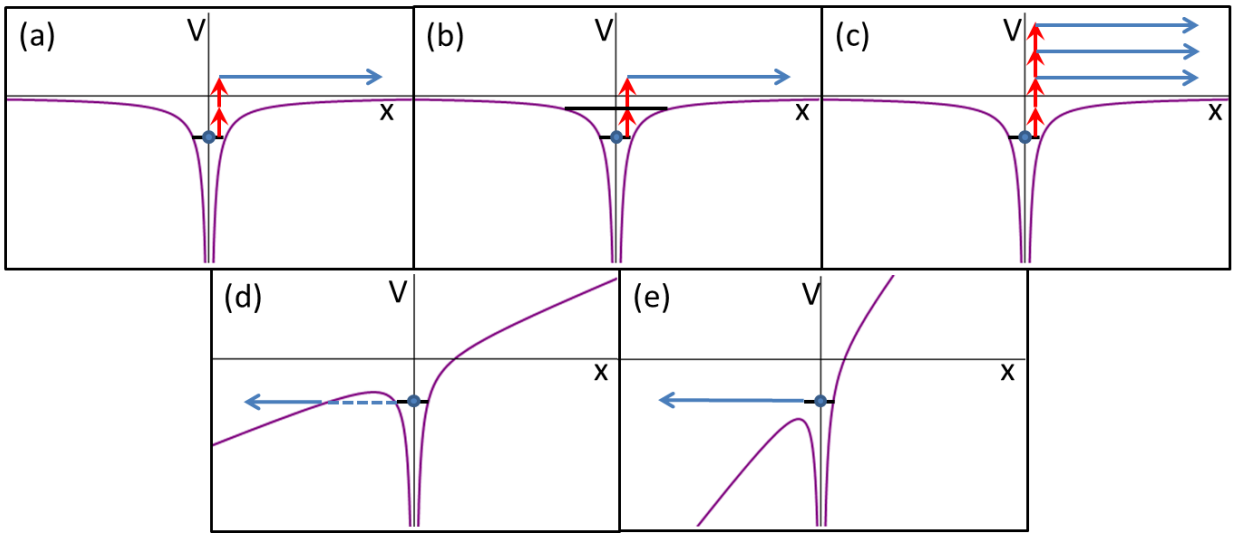

Figure 1.1 Illustrations of ionization mechanisms. (a) Multiphoton ionization (MPI); (b) Resonant enhanced multiphoton ionization (REMPI); (c) Above threshold ionization (ATI); (d) Tunneling ionization (TI); (e) Over the barrier ionization (OBI).

If the laser intensity is so strong ($I \geq 10^{14}$ W/cm^2) that the Coulomb potential starts to be distorted and oscillations with the external electric field occur, the electron might tunnel through

the laser-induced potential barrier [18], as indicated by Fig. 1.1(d). As the intensity is increasing, the barrier becomes lower and eventually, the electron can escape over the top of the barrier "classically", as indicated by Fig. 1.1(e). This regime is called over the barrier ionization (OBI) [10]. There is a critical intensity I_c for OBI to occur, which is

$$I_c = 4\times10^9 (I_p[\text{eV}])^4 Z_R^{\ 2} \qquad (1.4)$$

Here, Z_R is the residual charge of the atom or ion.

The Keldysh parameter γ is of great importance in ionization studies. It is defined by

$$\gamma = (\frac{I_p}{2U_p})^{1/2} \ . \qquad (1.5)$$

When γ <<1, the ionization occurs in the tunneling regime, while if γ>1, multiphoton processes will dominate, $\gamma \approx 1$ corresponds to a mixed regime. Since U_p is proportional to the laser wavelength, thus for longer wavelengths, the Keldysh parameter will be smaller. This means that tunneling processes are easier to establish in laser fields with longer wavelengths.

In the tunneling ionization (TI) or OBI regimes, the ionized electron might return to the vicinity of its parent ion driven by the external electric field. The returned electron acquires a significant amount of kinetic energy, recollides with the parent ionic atom or molecule, and can scatter (such as in non-sequential double ionization and above-threshold ionization) or recombine (such as in high harmonic generation). This three-step model has been introduced by P.B. Corkum and K. C. Kulander in 1993 [19, 20].

If the laser intensity is extremely high, the magnetic property of the laser field also has to be taken into account, and the electron spin becomes important [21].

Experimentally, photoelectron energy spectroscopy, angular resolved photoelectron spectroscopy, as well as ion yield measurements have been wildly used to investigate the characteristics of different ionization processes [1, 22-24, 86, 87]. Thanks to the development of experimental techniques such as the velocity map imaging (VMI), the angular distributions of the electrons can be detected [25, 27]. The photoelectron angular distributions (PADs) may be analyzed using a partial wave approach [28], which is further discussed in Chapter 4.

1.2 Organization of this thesis

The remainder of the thesis is organized as follows: The experimental setups are introduced in Chapter 2.

A phase controlled two-color laser field is used to explore the orientation dependence of the ionization of the CO and NO molecules, which is discussed in Chapter 3.

Chapter 4 describes our studies on C_{60}, a prototype for studies of complex molecules or clusters. In particular, we discuss experiments using about 30 fs laser pulses in the near-infrared and about 50 fs laser pulses in ultraviolet and compare them to the literature. The chapter closes with studies on the photoionization of C_{60}, where the chirp of the near-infrared laser fields is varied.

The last chapter gives an outlook for future work.

Chapter 2 - Experimental Setups

To study the photoionization of different kinds of molecules, our common experimental setups include a laser system and the consecutive optics to modify the laser field, a neutral gas phase molecular source, and a Velocity Map Imaging (VMI) system. The VMI system and the molecular source are in a vacuum chamber. The lasers we used in James R. Macdonald Laboratory (JRML) are high intensity ultrafast lasers providing pulses with time duration of about 30 fs. The laser beam is focused onto a molecular beam in a vacuum chamber, and the resulting ions or electrons are accelerated in an electrostatic field and velocity mapped onto a micro-channel plate (MCP) and phosphor assembly. The targets that we have studied include rare gases, such as Xe, heteronuclear molecules, such as CO and NO, and large molecules, such as C_{60}. In this chapter, I will introduce the experimental setups for the study of orientation dependence of the ionization of CO and NO, as well as the photoionization of C_{60}.

2.1 Laser systems

Nowadays, sub-30 fs intense ultrafast laser systems are commercially available and widely used in many labs around the world to study strong field and ultrafast atomic molecular physics phenomena. A typical laser system used is a Ti:sapphire chirped pulse amplifier (CPA) system [29]. A CPA system consists of four major parts, oscillator, stretcher, amplifier and compressor, which is shown in Fig. 2.1. The seed pulses generated in the oscillator are stretched temporally by the stretcher. This is to prevent the gain medium from being damaged in the next step. These stretched pulses will be amplified in a Ti:sapphire crystal, which acts as a gain medium. There are two types of amplifiers based on the geometry, multi-pass amplifiers and regenerative amplifiers. For the multi-pass amplifier, the laser beam will pass the gain medium several times along different traces. For the regenerative amplifier, the laser beam goes along the same path in a roundtrip in a cavity. At last, the pulses will be compressed in the time domain by the compressor. The output pulses will maintain high intensity as well as short duration.

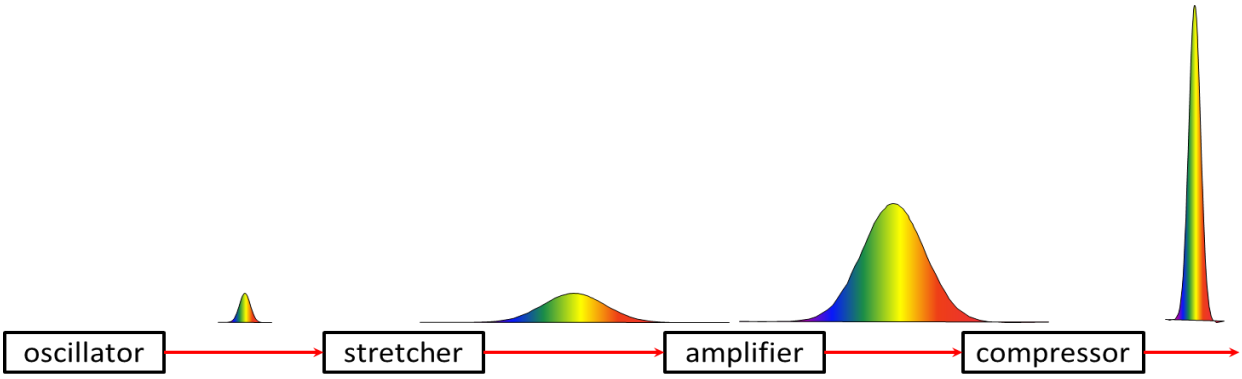

Figure 2.1 Diagram of the principle of a CPA system.

All the experimental work presented in this thesis is carried out at JRML at Kansas State University. Two femtosecond laser systems are used in our work. One of them is a home-built Ti:sapphire laser system, the Kansas Light Source (KLS), which was designed and built by Prof. Zenghu Chang's group. The other laser system is the Prairie Ultrafast Laser System for Attosecond Research (PULSAR), which was custom-built by KMLABS. The parameters of the two laser systems are given below.

2.1.1 Kansas Light Source (KLS)

KLS has been the main operating laser system at JRML during the last decade [88]. The final output pulses are 25~35 fs in duration with an energy of about 2 mJ/pulse at 2 kHz repetition rate. The central wavelength is about 790 nm. The oscillator of KLS is a Kerr-lens mode-locked Ti:sapphire oscillator. This oscillator generates 80 MHz, nano-joule level pulses with a bandwidth of about 80 nm. The pulses are selected by a Pockels cell and then input into a single-stage multi-pass amplifier. In the amplifier, the pulses are first stretched to tens of picoseconds, and then passed through a 14-pass loop. The gain medium in the amplifier is a Ti:sapphire crystal which is cooled by liquid nitrogen to reduce the thermal lensing effect. The amplified pulses are compressed by a pair of gratings at last. Fig. 2.2 is a photo of the amplifier of the KLS system at JRML. A frequency-resolved optical grating (FROG) system [89] is used for measuring the pulse durations for KLS.

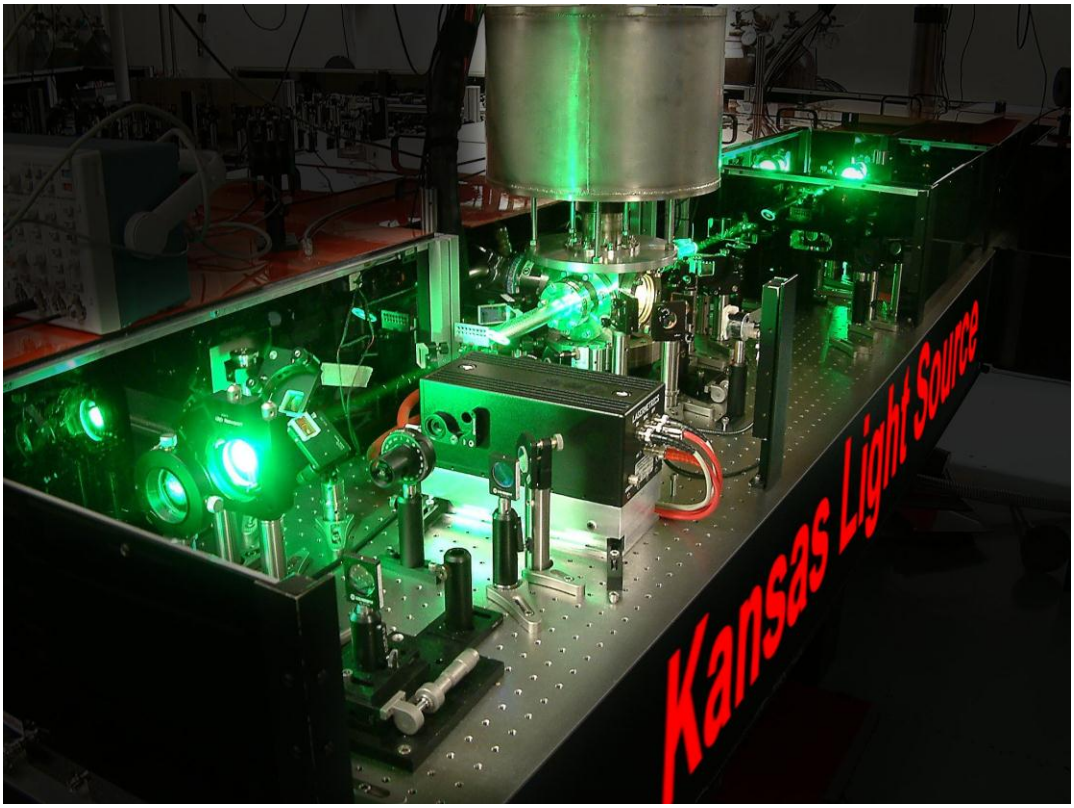

Figure 2.2 Photo of KLS amplifier. From http://jrm.phys.ksu.edu/script/beam-gallery.pl?KLS-Apr2006.

2.1.2 PULSAR

Recently, the PULSAR laser system was installed at JRML. PULSAR can generate shorter pulses with a duration down to about 21 fs, while operating at a higher repetition rate, i.e. 10 kHz. The laser can also be operated with 50 fs at 20 kHz. The central wavelength is about 785 nm. The maximum pulse energy is comparable to that of KLS, which is 2 mJ/pulse. The main part of PULSAR consists of an oscillator, a stretcher, a two-stage multi-pass amplifier, and a compressor. Besides, it has a pulse shaper and a carrier-envelope-phase (CEP) stabilization system for better control of the pulses. The layout of the whole system is shown in Fig. 2.3. The high repetition rate of PULSAR offers us a unique tool for the studies providing very low signal per laser shot and has thus been used for part of the work in my thesis on C_{60}. The data accumulation times are shortened dramatically. Besides, with the help of the CEP stabilization system, phase stabilized femtosecond pulses can be used to investigate dynamics as a function of the CEP. Alternatively, a recently implemented single-shot CEP-meter [30] allows for the

tagging of the CEP without active CEP stabilization. The pulses from PULSAR can be compressed down to around 4 fs with the help of a hollow-core fiber for spectrally broadening the pulse and chirped mirrors for their temporal compression.

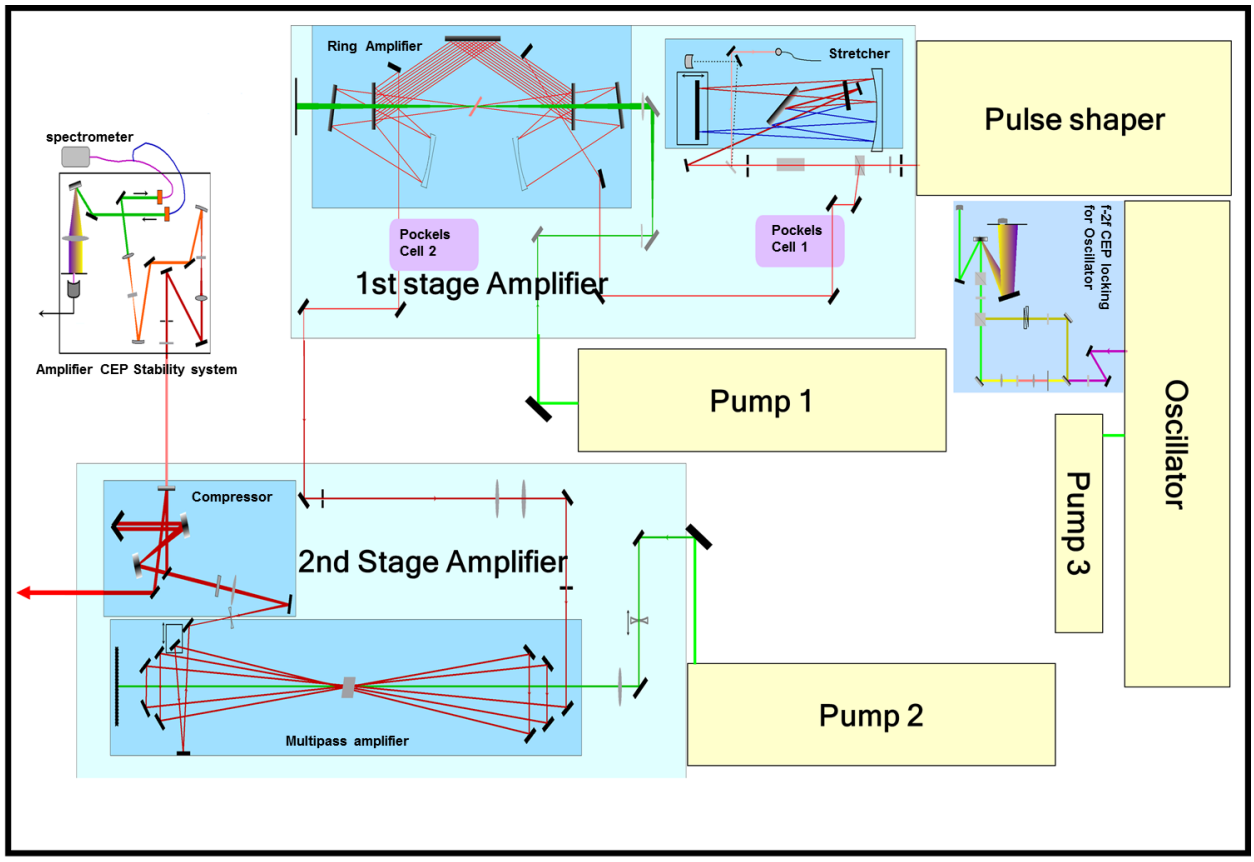

Figure 2.3 Layout of PULSAR system. [courtesy of Z. Wang].

2.1.3 Two-color setup

For the work presented in chapter 3 we used a two-color femtosecond laser field to study the orientation dependence of the ionization of CO and NO. The two-color field is generated in a collinear geometry with the help of a β-barium-borate (BBO) crystal [31-33, 37], which is shown in Fig. 2.4. Shooting an 800 nm infrared (IR) beam onto a BBO crystal, the second harmonic (SH) component at the wavelength of 400 nm can be created by the nonlinear effect in the crystal. Combining the IR beam with the SH component, we can get a controllable asymmetric field by tuning the relative phase between the two wavelength components. To some extent,

controlling the relative phase of the two-color component is comparable to controlling the CEP [35], however, in a much easier way.

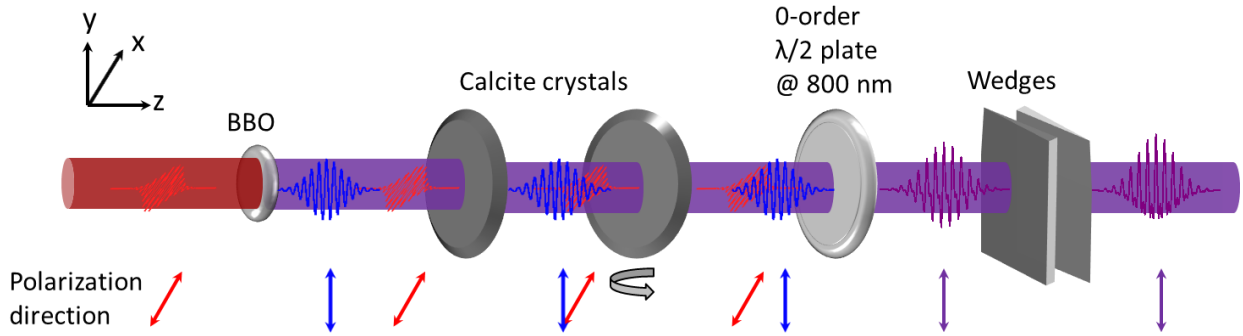

Figure 2.4 Schematic of the collinear two-color setup.

As is shown in Fig. 2.4, a beam of femtosecond pulses at the wavelength of about 800 nm, with pulse duration of about 35 fs is incident onto a BBO crystal. The second harmonic component at the wavelength of 400 nm is generated by nonlinear effects in the crystal. The thickness of the BBO crystal is 250 μm. The output 400 nm beam after the BBO crystal is polarized perpendicular to the polarization direction of the IR beam. In Fig. 2.4, the input IR beam is polarized along x-axis, while the SH beam is polarized along y-axis after the BBO crystal. The 400 nm pulse will be somewhat longer than the 800 nm component, and they have a time delay of about 60 fs after the BBO. The intensity of the 400 nm pulse is typically 10 ± 3 % of that of the 800 nm field at the optimized condition. Most of the optics materials as well as the air provide normal group velocity dispersion (GVD), i.e. the longer wavelength travels faster than the shorter wavelength. To compensate for the normal GVD, we use two birefringence calcite crystal plates in such a way that the longer wavelength component oscillates along the slow axis, while the shorter wavelength component oscillates along the fast axis. One of the calcite crystals is rotatable to adjust the relative phase shift between the two color components. After the calcite crystals, the beam passes through a zero-order half wave plate at the wavelength of 800 nm. It acts as a half wave plate for 800 nm, rotating the polarization direction by 90 degree. However, this wave plate acts like a full wave plate to the 400 nm component without changing its polarization direction. Both 800 nm and 400 nm components are polarized along the y-direction after the wave plate. A pair of fused silica wedges is used to further optimize the time

delay of the two wavelengths. By now, a beam of asymmetric femtosecond pulses is ready to be sent to the interaction vacuum chambers, such as a VMI chamber.

The electric field of a two-color pulse can be given by

$$E(\mathrm{t}) = E_1(t)\cos(\omega t) + E_2(t)\cos(2\omega t + \varphi)\,. \tag{2.1}$$

Here $E_1(t)$ and $E_2(t)$ are the temporal envelopes of the electric field of the fundamental IR and SH components, respectively, ω is the angular frequency of the input beam, and φ is the relative phase between the two color components. For different phase shifts, we will get different pulse shapes. Fig. 2.5 shows some examples of the two-color pulses for different phase shifts, with Gaussian profile in time domain.

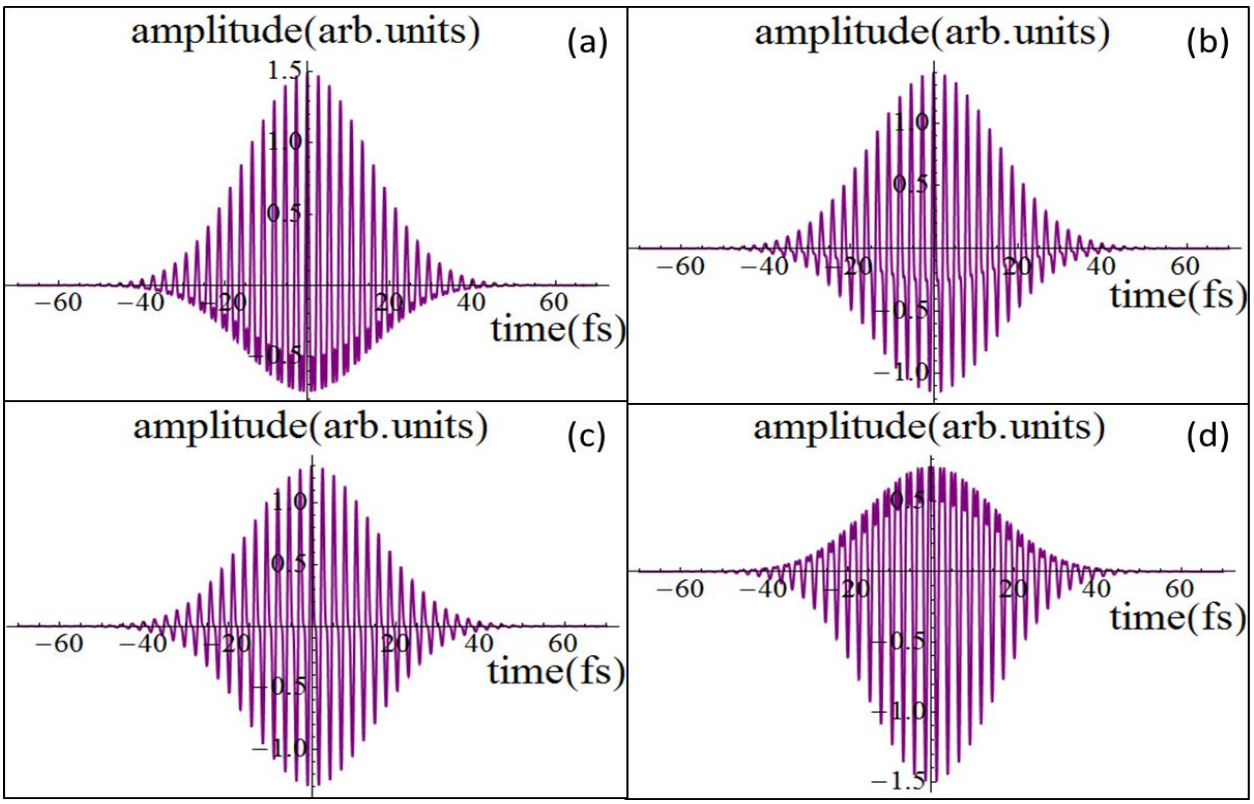

Figure 2.5 Two-color pulse shapes for different relative phase between the fundamental and SH component. Here, FWHM = 30 fs, $E_2 = E_1/2$, λ = 800 nm. (a) $\varphi = 0$; (b) $\varphi = \pi/3$; (c) $\varphi = \pi/2$; (d) $\varphi = \pi$.

In our experiment, one of the calcite crystals is mounted onto a rotational stage which is controlled by the computer. By scanning the rotational angle step by step, we get the signal under

the two-color laser field with respect to different phase shifts. Fig. 2.6 shows a typical VMI image of the photoelectron emission from Xe under an asymmetric two-color laser field with the phase shift φ ~0.

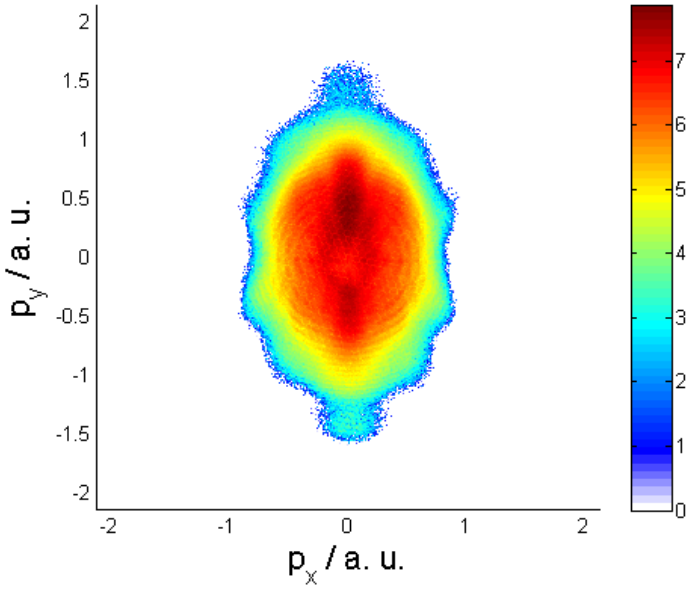

Figure 2.6 VMI image of the photoelectron from Xe under an asymmetric femtosecond two-color laser field for $\varphi \approx 0$.

2.2 Velocity map imaging system

In 1997, André T. J. B. Eppink and David Parker published a paper on the velocity-map imaging (VMI) method, whose operation principle has been used for the VMI applied in our work. Combining an electrostatic lens and 2D detection, the instrument opened a new era for the study of atomic molecular physics [25].

The VMI system used in our work was designed by N. Kling (former name N. G. Johnson) and S. De and has been used in many studies at JRML [32, 34, 37]. Using the SIMION software, the electric field, the equipotential surfaces, as well as the trajectories of charged particles have been mapped out under different electrostatic lens geometries and different initial conditions by N. Kling. Our VMI spectrometer is schematically shown in Fig. 2.7.

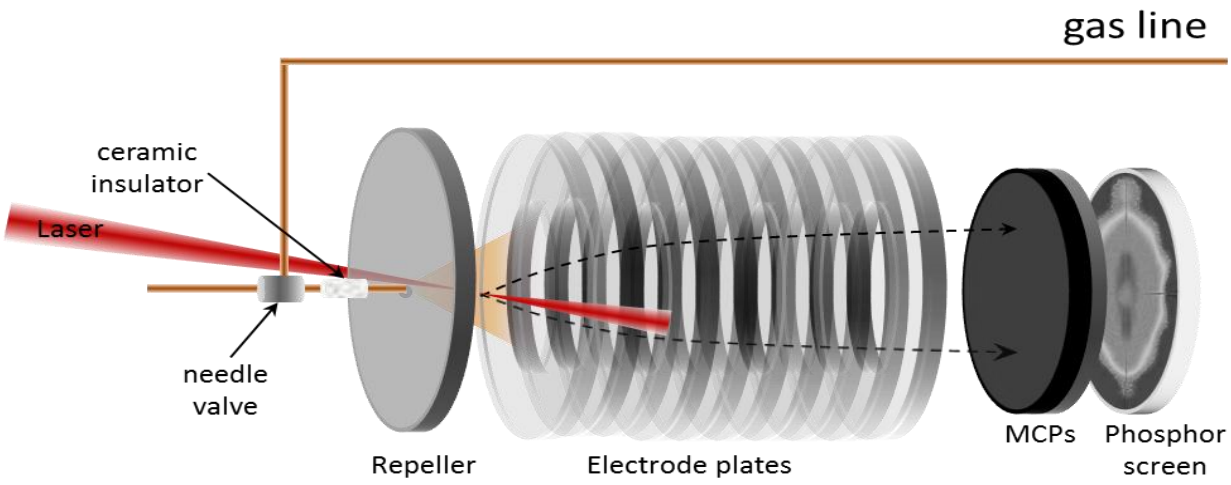

Figure 2.7 Schematic diagram of the VMI system.

The electrostatic lens contains 11 electrodes which generate a static electric field guiding the ions or electrons to the detector in such a way that those with the same initial transverse velocity (parallel to the detector surface) end up on the same point on the detector. The repeller is a metal plate with a 30 μm (diameter) hole at the center. This small hole produces an effusive gas jet. The input gas pressure is controlled by a needle valve in the gas line before entering the jet. A ceramic insulator is installed between the repeller and the gas line to insulate high voltage on the repeller. Other electrodes are all annular plates. We apply voltage on the first four plates, the repeller, the 2^{nd}, 3^{rd} and 4^{th} plate. The voltage applied on the 4^{th} plate should be 80% of that applied on the repeller. The voltages on the 2^{nd} and 3^{rd} plate are scaled such that there is equal voltage difference among the first four plates. The last electrode plate is grounded. All the other plates are connected to their neighbors by equal resistance. With such an electrostatic field, the particles with the same velocity formed inside the small interaction region will be mapped onto the same point on the MCP.

The detector consists of a pair of MCPs and a phosphor screen. A more specific illustration of the detector assembly is shown in Fig. 2.8. The MCPs are responsible for the signal amplification while the phosphor screen transfers the electron pattern into a visible pattern by fluorescence. The MCP is made of millions of thin, glass capillaries fused together and cut into the shape of a thin plate. Each capillary forms a channel, working as an independent secondary-electron multiplier. All the channels are tiled in a bias angle (8^{o} for our MCPs) with respect to the surface normal direction. The incident charged particles hitting the channel wall

will emit secondary electrons. By hitting the wall several times, the number of electrons is dramatically amplified. These electrons will be accelerated by the electric field applied across the MCPs. A large amount of electrons released from the output surface fly onto the phosphor screen, generating fluorescence and providing a visible image which can be recorded by a camera. Our MCPs (model 75/32/25/8) are purchased from PHOTONIS. For better control of the signal gain, we installed several electrode contacts including MCP front, MCP middle, MCP back and Phosphor, which are shown in Fig. 2.8.

There are two different modes that the system can work in, the ion time of flight (TOF) mode and the VMI mode. For the TOF mode, positive voltages are applied to the electrode plates to accelerate the ions to the detector. Different ion species with different charge mass ratios will arrive at the detector at different times. We apply a higher voltage on the phosphor screen than that is applied to the MCPs, to make sure that all the amplified electrons coming out from the MCP back surface will hit the phosphor screen at last. The signal from the phosphor screen is input into a telescope through a decoupling box. The trigger signal is taken from the laser pulses by a photodiode. According to the TOF spectrum, a time delay for a specific ion species can be determined. This will be further used for taking the VMI measurement for certain ions.

In VMI mode, momentum imaging of either electrons or ions can be realized. For ion VMI mode, by gating the MCP using a laser-triggered high-voltage switch at an appropriate delay, which is determined in TOF measurement, specific ions can be imaged. Typically, the voltages applied across the two MCPs are about 1.6 kV to 2.0 kV. The voltage on the phosphor screen is 2 kV higher than that applied on the MCP back. The gain of the MCP is very sensitive to the bias voltage. To get maximum gain, it is ideal that the voltages across each MCP are equal. However, the resistance of two MCPs might not be the same. If we apply voltage on MCP front and MCP back, the voltage drop over the two MCPs might deviate. In our setup, for instance, we can ground the MCP middle, apply -800 V on MCP front, +800 V on MCP back, and 2800 V on Phosphor, to make sure that the two MCPs maintain the same bias. If the experimental condition is not so restrict, we can simply ground the MCP front, and apply 1.6 kV on MCP back, 3.6 kV on Phosphor, with MCP middle floated. Usually, the signal can be amplified by a factor of 10^6 with the two MCPs. For electron VMI mode, negative voltages are applied to the repeller and the electrode plates to accelerate electrons. It is hard to distinguish the electrons from target and electrons from background by gating the MCPs. Thus the chamber vacuum becomes a crucial

factor for electron detection. For our experiment, the chamber background is maintained at 10^{-9} Torr or lower. Raw VMI images of C^+ ions from CO and images of photoelectrons from Xe are shown in Fig. 2.9 (a) and (c).

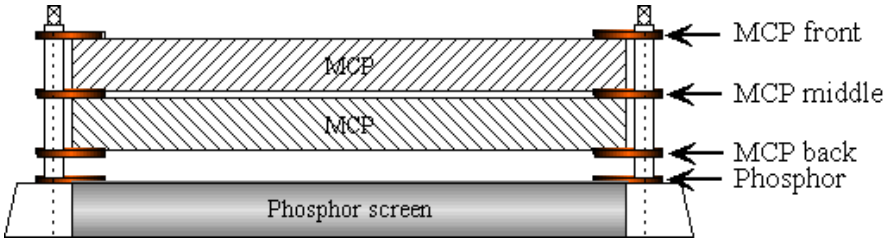

Figure 2.8 Diagram of the MCP and phosphor assembly.

The spectrometer is shielded by a μ-metal shell, to avoid the influence from the magnetic field of the earth and stray magnetic fields in the laboratory. The whole VMI system is mounted onto a 10" flange and installed in a vacuum chamber. The vacuum that can be reached without gas flow is about 10^{-10} Torr while the typical values with gas flow is about 10^{-8}~10^{-7} Torr. A photo of our VMI system is shown in Fig. 2.10.

The laser beam is focused onto the gas target through the gap between the repeller and the 2nd plate, as shown in Fig. 2.7. After light matter interaction, the resulting ions or electrons are guided to the detector by the static electric field. The two dashed curves in Fig. 2.7 are typical trajectories for the charged particles in the spectrometer. The particles are incident onto the MCP, amplified, and then visualized on the phosphor screen. From the 2D momentum images, we can extract the 3D information of the kinetic energy and angular distribution by means of an iterative inversion procedure [27]. Fig. 2.9 shows VMI images of C^+ ions from CO and images of photoelectrons from Xe before and after inversion.

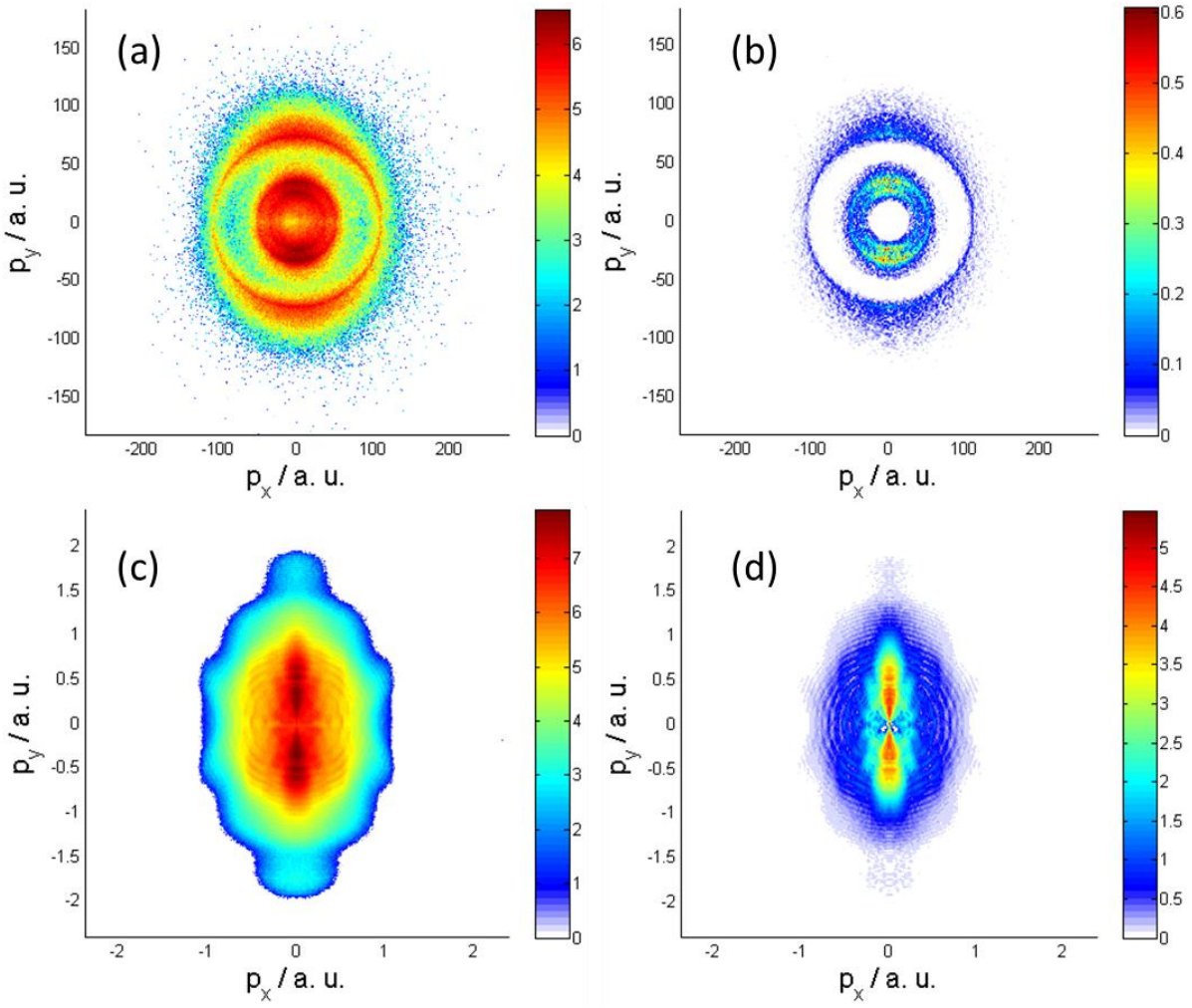

Figure 2.9 VMI images of (a) C^+ ions from CO: raw image; (b) C^+ ions from CO: image after inversion; (c) photoelectrons from Xe: raw image; (d) photoelectrons from Xe: image after inversion.

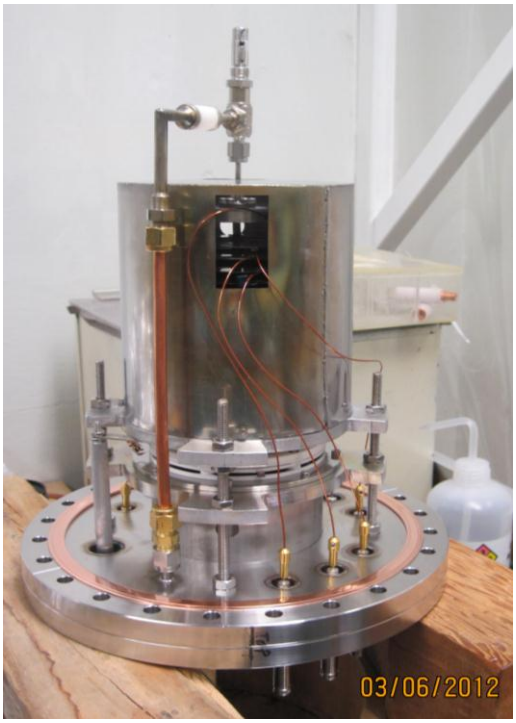

Figure 2.10 Photo of our VMI system.

2.3 C_{60} beam source

We use an effusive neutral C_{60} beam source for our ionization studies in femtosecond laser field. Our C_{60} beam is produced from a home-made oven mounted inside the VMI vacuum chamber. A sketch diagram of the oven is shown in Fig. 2.11.

The main part of the C_{60} source includes an oven and a shield. The cylindrical oven is made of stainless steel, and surrounded by a cable heater. A thermo-couple is installed at the top inside the oven. Because our oven is mounted on the top flange and the C_{60} beam shoots downward, we build a reservoir for C_{60} soot. The C_{60} soot used in our experiment is 99.9% highly crystalline sublimed fullerene from Sigma Aldrich. The vapor pressure of C_{60} under different temperature has been well studied [36]. To get enough photoelectron signals, the oven needs to be heated up to about 450 ^{o}C ~ 600 ^{o}C, depending on the specific experimental conditions. Fig 2.12 shows the yield of C_{60}^{+} and C_{60}^{2+} ions under the laser intensity of about 2×10^{13} W/cm^2 for 45 fs pulses from KLS versus different oven temperature, compared to the vapor pressure reported in ref. [36]. The shield is made up of two co-axis metal cylinders. Large holes (indicated by the dashed lines in Fig. 2.11) on the two layers of the shield allow for vacuum pumping. Ceramic insulators between the oven and the shield prevent heat transfer.

There is an effusive hole at the bottom of the oven with a diameter of 2 mm. When the vapor pressure inside the oven is high enough, the gas phase C_{60} will be ejected through the small hole. The other 2 mm hole at the bottom of the shield is to collimate the C_{60} beam. C_{60} molecules emitted under large angles after the first hole will be collected by the shield.

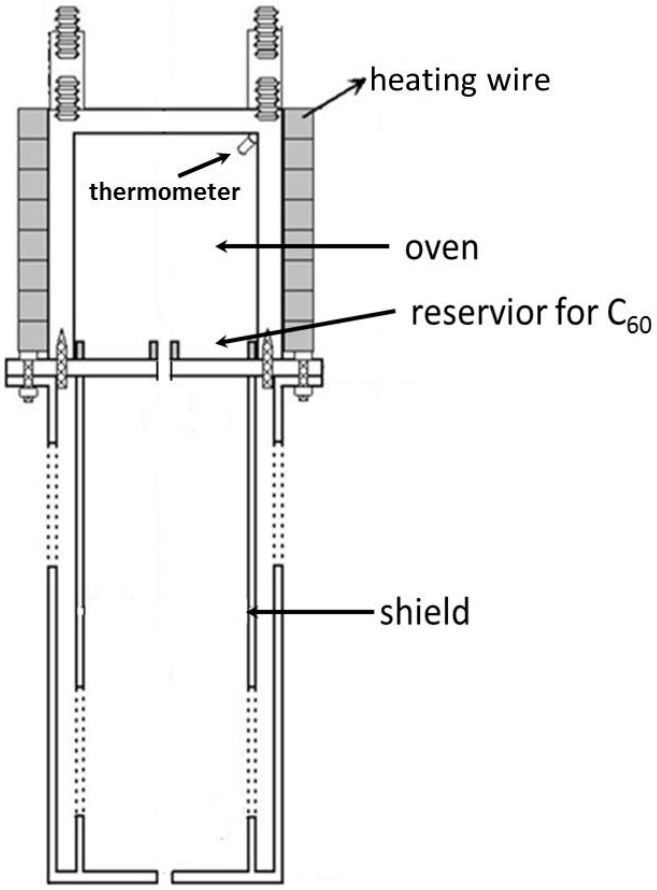

Figure 2.11 Sketch diagram of the C60 oven. For details see text.

The C_{60} source is installed on a 6" flange and mounted in the VMI chamber. The C_{60} beam, the laser beam and the VMI spectrometer axis form an orthogonal geometry as shown in Fig. 2. 13.

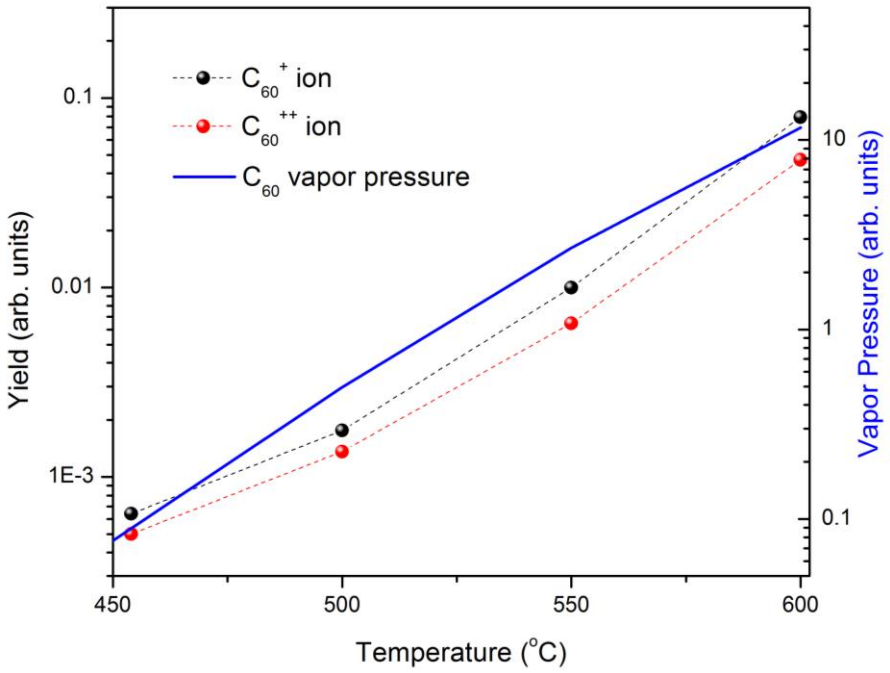

Figure 2.12 C_{60}^{+} and C_{60}^{2+} yield and C_{60} vapor pressure vs. temperature. The black bullets and red bullets are the yield of C_{60}^{+} and C_{60}^{2+} ions under laser intensity of 2×10^{13} W/cm^2, respectively. The blue curve is the vapor pressure of C_{60} reported in ref. [36].

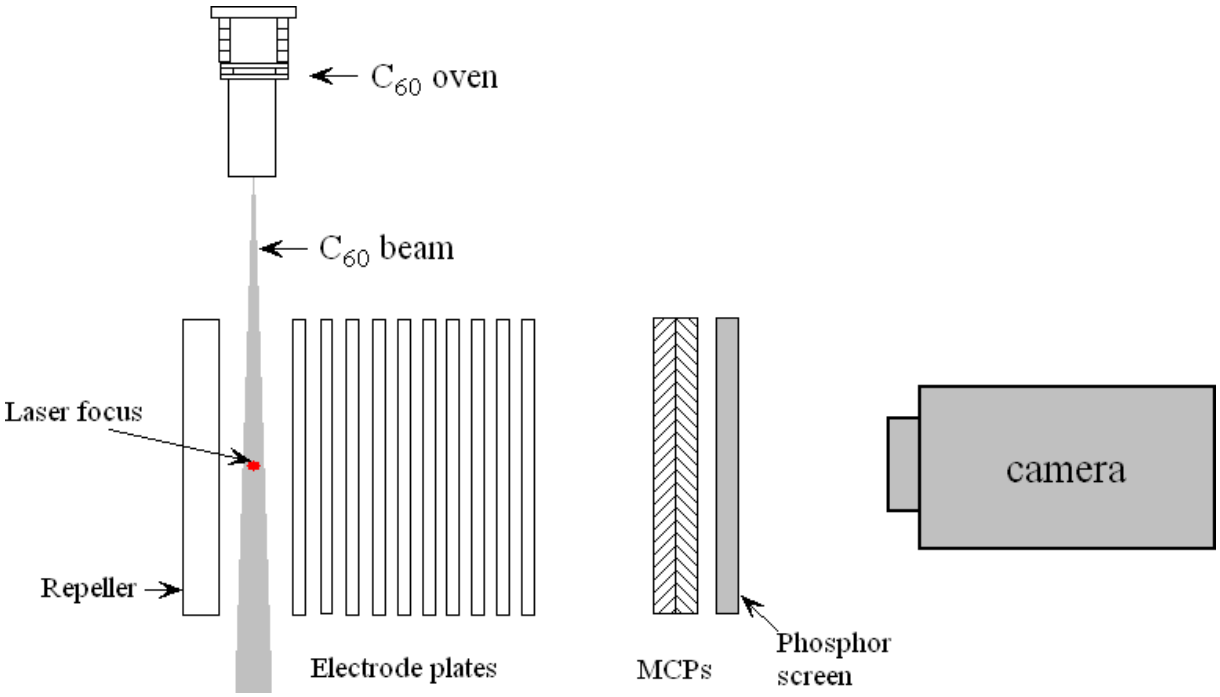

Figure 2.13 Sketch of the geometry using the C_{60} source together with the VMI in our laser experiments.

Chapter 3 - The orientation dependence of the ionization of CO and NO in two-color laser fields

In this chapter, results on the orientation dependence of the ionization of the heteronuclear molecules CO and NO in two-color laser fields are discussed. Two-color femtosecond, linearly polarized pulses are produced with the collinear setup discussed in section 2.1.3. The fundamental frequency component is a beam of 35 fs pulses from KLS with a central wavelength at about 800 nm at a 2 kHz repetition rate. The second harmonic component at the wavelength of 400 nm is generated and then interferometrically combined with the 800 nm radiation to provide a two-color field $E(t) = E_1 \cos(\omega t) + E_2 \cos(2\omega t + \varphi)$. The two-color fields, controlled by the relative phase φ, are used to ionize and dissociate CO and NO molecules, both of which are molecules with small polarizabilities. The resulting C^+, C^{2+}, N^+ and O^+ ions are detected by a VMI setup. The photoelectrons from above-threshold ionization (ATI) of Xe are studied under such a two-color field to assign the absolute phase. For both CO and NO we find that enhanced ionization occurs when the molecule is oriented with the electric field pointing from the C or N atom toward the O atom. This is in agreement with the molecular orbital Ammosov-Delone-Krainov (MO-ADK) theory and the Stark-corrected strong-field-approximation (SFA) calculations [37].

3.1 Introduction

The ionization rate of atoms or molecules in an intense laser field is well studied (see e.g. [38, 39]). For diatomic molecules, the ionization rate depends on the angle between the laser polarization direction and the molecular axis. A convenient treatment for this case is the MO-ADK theory [40], which predicts an enhanced ionization rate of an orbital, usually the highest occupied molecular orbital (HOMO), to occur when the molecule is aligned with its orbital angular maxima along the laser polarization. A number of experiments using momentum imaging techniques have been carried out to measure the angular dependence of the ionization rate for small molecules with linear polarization [41, 42] or circular polarization [43-45], as well as impulsive and adiabatic pre-alignment [32, 46-48]. The shape of the HOMO can be mapped

out by measuring the ionization rate [35, 41-43, 46, 47, 49, 50]. For heteronuclear molecules, MO-ADK theory predicts that the ionization rate is orientation dependent rather than alignment dependent. Several experiments have measured the orientation dependence of the ionization rate of some molecules [44, 45, 48, 51]. In some cases, the orientation dependence is attributed to the effective ionization potential of the HOMO (or HOMO-1) (Stark shifted) of the molecule [44, 45]. This dependence comes from the dipole energy of the interaction between both neutral and ionized molecule and the electric field. Surprisingly, if we include the effect of the linear Stark effect, the higher ionization will occur at just the opposite orientation from what is predicted by the MO-ADK theory [52].

There are some recent theoretical studies on the orientation dependence of the ionization rate [48, 52-54]. For small molecules with low polarizabilities, the MO-ADK theory, modified by a linear Stark shift correction of the ionization potential, is found to be adequate. The preferred orientation of the ionization will not change compared to what is predicted by MO-ADK theory; however, the rate would be weakened by the linear Stark effect. For molecules with large polarizabilities, this approach is not sufficient anymore. The electron distribution around the molecule tends to change with the electric field, which requires a more complete treatment. In Ref. [48], a simple model is provided to predict the favored ionization of carbonyl sulfide (OCS) for an orientation just opposite to what predicted by MO-ADK theory.

There is another problem when considering the orientation dependence of the ionization rate of heteronuclear diatomic molecules. That is, which way do the electrons preferentially go? If we find out the favored orientation direction of the molecule for maximum ionization, we know which way the electron is initially extracted, i.e., opposite to the field direction, because electrons are negatively charged. However, this might not be the direction in which the electrons are finally detected. In a strong-field picture, the final momentum of a “direct” (non-backscattered) electron is determined by the vector potential at the time when it tunnels out, which is typically when the vector potential is passing through zero. Thus it is not easy to distinguish the direction of the vector potential when the electrons are emitted, and the direction of the field is hard to determine by the “direct” electrons. Some studies on the electrons from Xe in a two-color field [33, 37] show that the backscattered electrons occupying the high energy part of the plateau behave in a very intuitive way which can be used to determine the two-color phase and, thus, determine the direction of the electric field. For instance, when the electrons are

preferentially extracted to the left, the backscattered electrons will also end up in the left direction. In this chapter, we use electrons from Xe to assign the absolute two-color phase. Furthermore, by comparing the asymmetry behavior of electrons from the spherically symmetric atom Xe and the diatomic molecule CO in a two-color field, we find that they are quite similar. This indicates that in this case the structure of the emitter does not play a large role for the electron dynamics after extraction.

The intensity of the 400 nm component is typically around (10 ± 3) % of that of the 800 nm field. The two-color field is focused onto an effusive gas jet of Xe, CO or NO inside a VMI system. The electrons or ions after the laser-matter interaction are detected with the VMI. The momentum images are Abel inverted and energy spectra or directional asymmetries generated for further analysis.

3.2 Assignment of the absolute two-color phase from photoelectron spectra of ATI in Xe and emission of electrons from CO in an intense two-color laser field

Previous studies show that the rescattering photoelectrons from Xe in a two color field have a strong dependence on the two color phase [33]. Both calculations based on solving the time-dependent Schrödinger equation (TDSE) and from the quantitative rescattering (QRS) theory [55] indicate that, in comparison to direct electrons, the rescattered electrons provide a more reliable method to assign the absolute two-color phase. We have therefore followed this procedure and used the rescattered electrons from Xe to assign the two-color phase.

The Xe electron VMI spectra are obtained as a function of the phase between the two colors. We adjust the phase by controlling the rotation angle of one piece of calcite crystal about its optical axis using a computer-controlled rotation stage. The rotational angle and the corresponding phase shift of the two color field are not in a linear relationship. The time delay between the 800 nm and 400 nm component in the calcite crystal is given by

$$\Delta t = \frac{\Delta n \times d}{c} \ . \qquad (3.1)$$

Here Δt is the relative time delay between the IR and blue components, $2\pi \times \Delta t / T$ is the corresponding phase shift, where T is the optical cycle of the IR beam. Δn is the refractive index difference of the calcite crystal between 800 nm and 400 nm, d is the thickness of the crystal, and c is the speed of light in vacuum.

When the calcite crystal is rotated by an angle of θ, as indicated in Fig. 3.1, the thickness will change with the angle by

$$\Delta d = d' - d = \frac{d}{\cos\theta} - d \qquad (3.2)$$

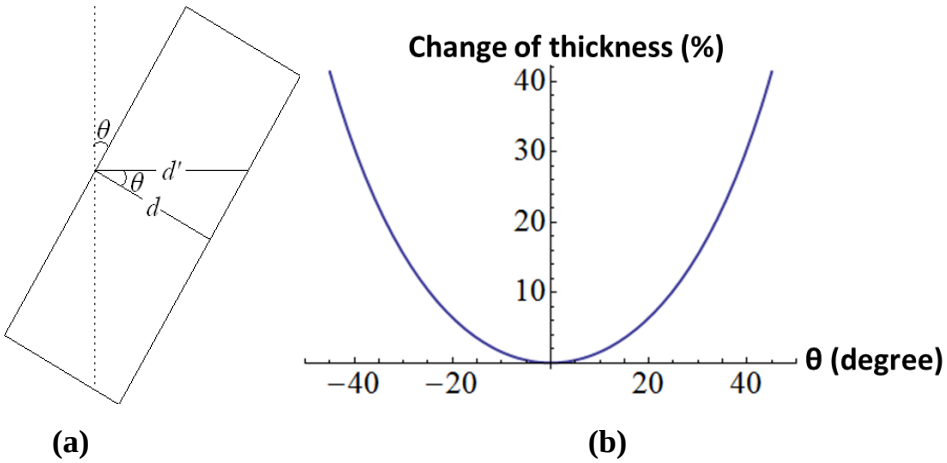

Figure 3.1 (a) Illustration of the thickness dependence on rotational angle. (b) Plot of the change of thickness of the calcite crystal versus rotational angle.

Fig 3.2 shows a density plot of the directional asymmetry along the laser polarization axis of the electron emission from Xe as a function of the two-color phase φ and the electron energy. The asymmetry of Xe electrons is defined by (Y_{up}-Y_{down}) / (Y_{up}+Y_{down}), where Y is the electron yield. The laser polarization is vertical. In the analysis, the yield is obtained by integrating the spectrum within an angle of 15^{o} with respect to the laser polarization axis (y-axis) to each side. The rescattered electrons are located in the energy range from about 30 eV to 50 eV [56]. It is very clear from the plot that the asymmetries for direct and rescattered electrons are different. Furthermore, we can see that the asymmetry becomes saturated for the higher energy range since the signal in this range is much lower compared to the direct electrons, which is indicated by the upper left panel in Fig. 3.2. Therefore, the rescattering electrons are not so easy to be recognized on the asymmetry density plot due to the saturation. However, we find a better way to do that by

comparing the density plot of electron yield with the theoretical calculation of the yield from a solution of the TDSE.

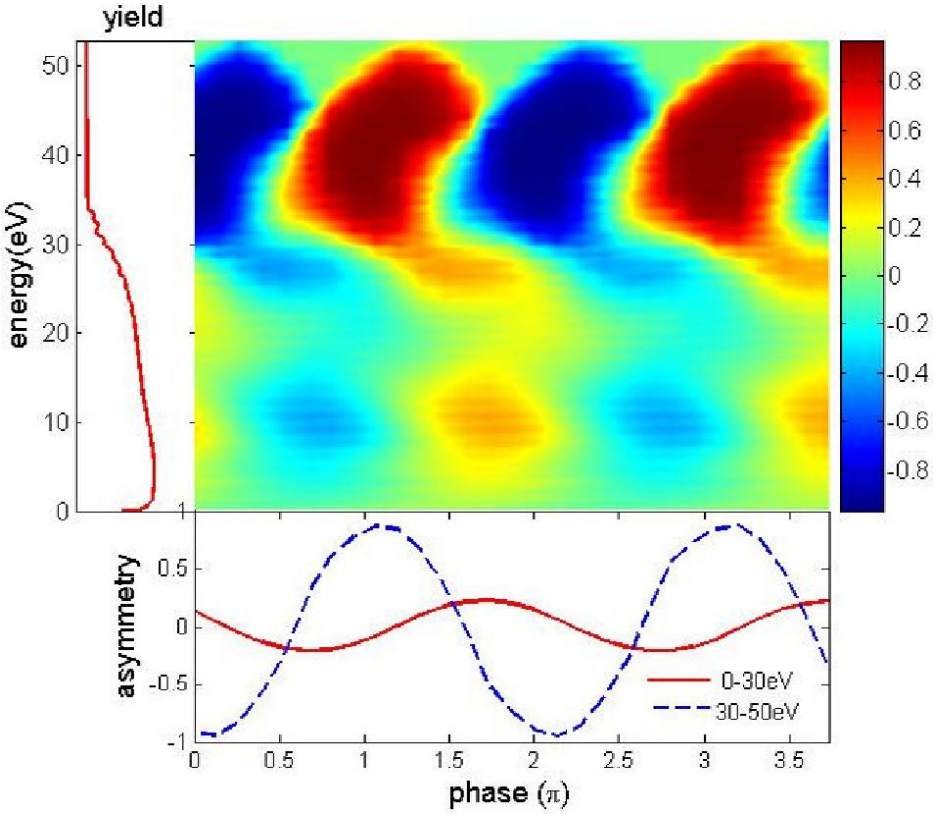

Figure 3.2 Density plot of the measured asymmetry of the electron emission from Xe at an intensity of about 0.7×10^{14} W/cm^2 as a function of electron energy and two-color phase φ. The upper left panel is a projection of the yield versus the electron energy in logarithmic scale. The bottom panel shows plots of asymmetry versus phase for two chosen energy slices. From Ref. [37].

Fig. 3.3 shows a comparison of the electron yield in the down direction to the TDSE calculation result for this process [33]. This comparison provides us with a tool to assign the absolute two-color phase. The characteristic hook-shaped pattern can be used to identify the rescattering region. The absolute zero phase for the two-color field locates at about $\pi/2$ before where the maximum electron energy occurs. Also, the ratio of the electric field amplitude of the 400 nm and 800 nm components E_2/E_1 can be deduced to be 0.2 ± 0.08 from this figure. All the two-color phases in this chapter are assigned on the basis of this comparison.

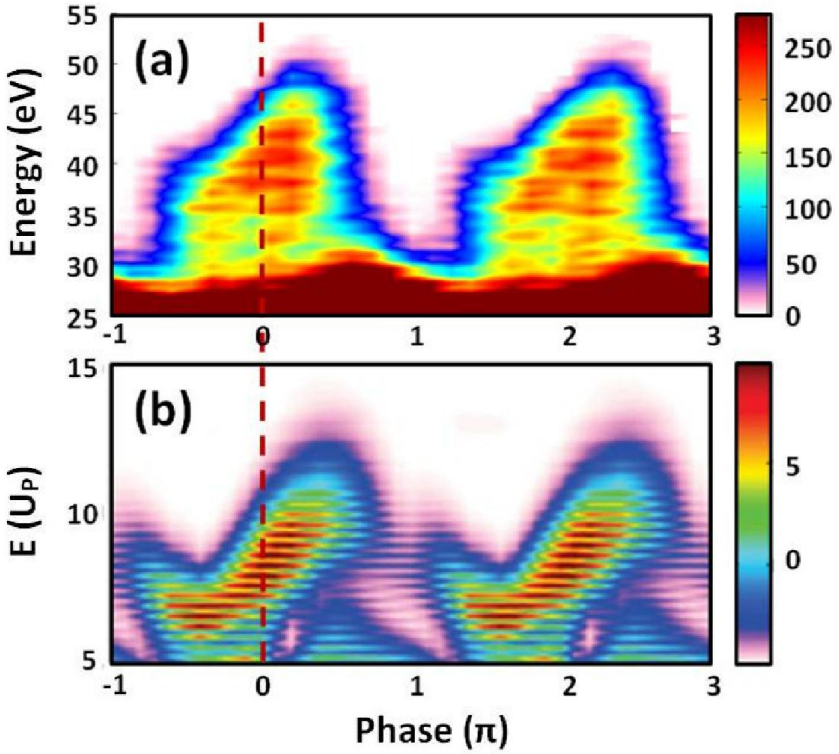

Figure 3.3 (a) Density plot of measured "down" electron yield as a function of the electron energy and the two color phase. (b) TDSE calculation for similar conditions. From Ref. [37].

Fig. 3.4 gives an illustration of how the VMI images for photoelectrons change with respect to different two-color phases. Here electrons from Xe as well as from CO are shown. The backscattered electrons from CO are not so distinct as those from Xe. However, the characteristic hook shape for the backscattered electrons can also be identified for CO in the density plot of the electron yield in the down direction, as is shown in Fig. 3.5. Furthermore, Fig. 3.6 shows the density plot of the asymmetry of the electron emissions for a CO target.

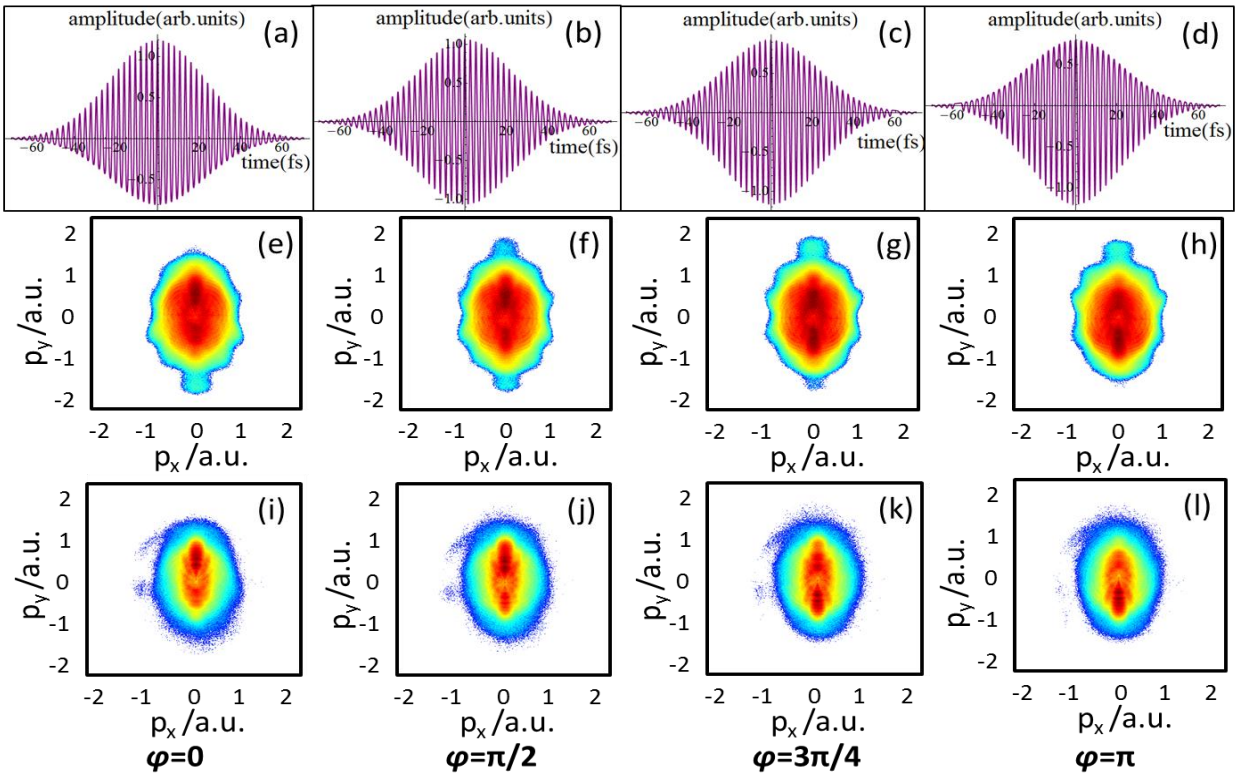

Figure 3.4 Two-color fields and photoelectron VMI images from Xe and CO under different phases. (a-d) Sketches of two-color fields for phases φ of 0, $\pi/2$, $3\pi/4$ and π. (e-h) Corresponding raw VMI images for electrons from Xe at a laser intensity of about 0.7×10^{14} W/cm^2. (i-l) Raw VMI images for electrons from CO at a laser intensity of about 0.7×10^{14} W/cm^2.

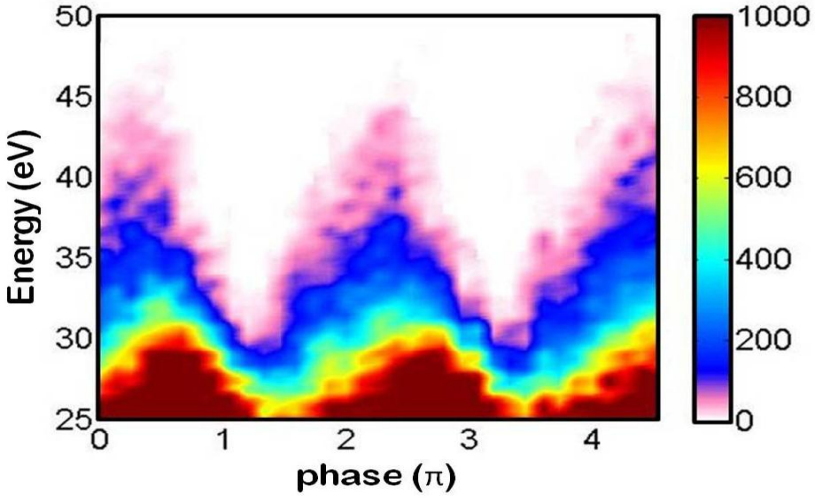

Figure 3.5 Density plot of measured "down" electrons as a function of the electron energy and the two color phase for a CO target. From Ref. [37].

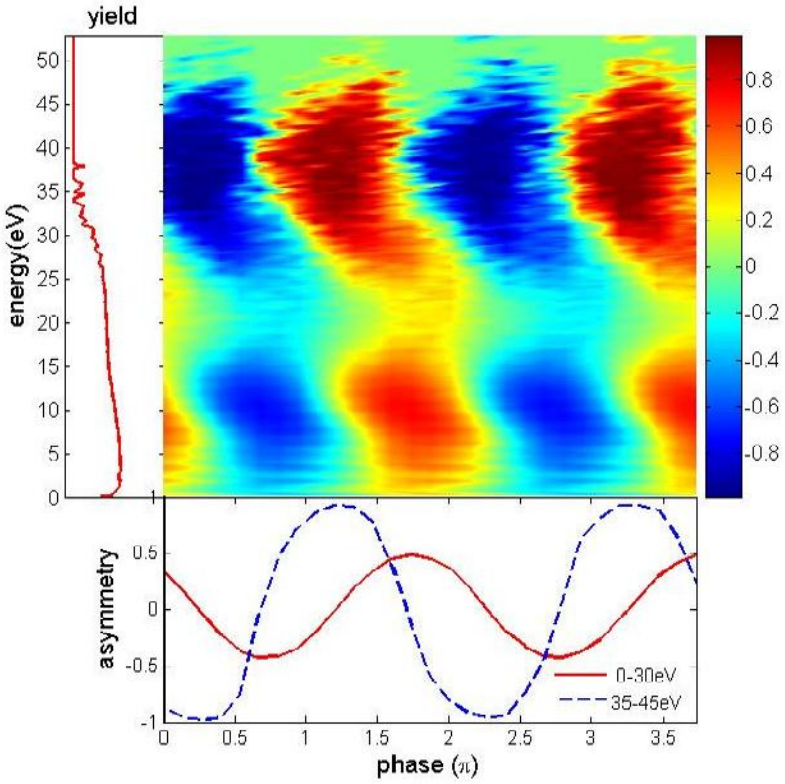

Figure 3.6 Density plot of the asymmetry of the electron emission from CO at an intensity of about 0.7×10^{14}W/cm^2 as a function of electron energy and two-color phase φ. The upper left panel is a projection of the yield versus the electron energy in logarithmic scale. The bottom panel shows plots of the asymmetry versus phase for two chosen energy slices. From Ref. [37].

The backscattered electrons have their intuitive behavior. At the phase $\varphi = 0$, the electric field points up. Electrons extracted from the parent move downward, rescatter, and end up in the down direction. This agrees with what is shown in Figures 3.2 and 3.6: at zero phase, the asymmetry almost reaches the maximum absolute negative amplitude for the rescattered electrons within the energy range of about 35 eV to 50 eV. Also from these figures, we can see that the direct electrons behave differently compared to the higher energy rescattered electrons. At the same phase, when the electric field points up, the direct electrons with lower energy are preferentially observed in the up direction, indicated by the positive asymmetry values for an energy range of 0 to 30 eV. These direct electrons are influenced by the electric field as well as the molecular potential. The combined action sends the electrons to the opposite direction to that

of the rescattered ones. Fig. 3.6 looks very similar to Fig. 3.2. Although the electrons are from different targets, their asymmetry behaviors are quite similar. This indicates that the structure of the CO molecule does not strongly affect the asymmetry behavior of emitted electrons in this case.

3.3 Asymmetry of ion yields of CO and NO in an intense two-color laser field

After studying the asymmetry behavior of the electron emission and assigning the absolute two-color phase, we have measured the asymmetry of ion yields of two kinds of heteronuclear molecules, CO and NO, both of which exhibit small polarizabilities.

By gating the MCP using a laser-triggered high-voltage switch at an appropriate delay, specific ions can be imaged. Fig. 3.7 shows the density plot of asymmetry of C^+ ion yield from CO as a function of their kinetic energy release (KER) and two-color phase. The plot of yield versus KER is shown at the upper left panel, while the projections of asymmetry versus phase of two energy slices are shown in the lower panel. The groups near 1 eV and 6-8 eV correspond to dissociation of the CO molecule into C^+/O and C^+/O^+, respectively. Many dissociative states are involved in each case, as discussed in Refs. [35, 42, 57-60]. The asymmetry of the emission of the C^+ ion for the C^+/O^+ channel shows very little KER dependence. The asymmetry for the C^+/O channel has nearly the same phase as the double ionization channel over most of the KER range with weaker asymmetries. The agreement in the sign and phase of the asymmetry supports the supposition that the asymmetry is mainly determined by the removal of the first electron from the CO molecule. Figures 3.8 and 3.9 further support this supposition by showing similar plots for C^{2+} and O^+ ions. The plot for C^{2+} ions shows a similar pattern as that for C^+ ions, while the O^+ ions exhibit opposite pattern in asymmetry. This agrees with the assumption that the orientation of the CO molecule in the removal of the first electron mainly determines the asymmetry. From Figures 3.7, 3.8 and 3.9, we see that the maximum asymmetries appear near phase 0 and π.

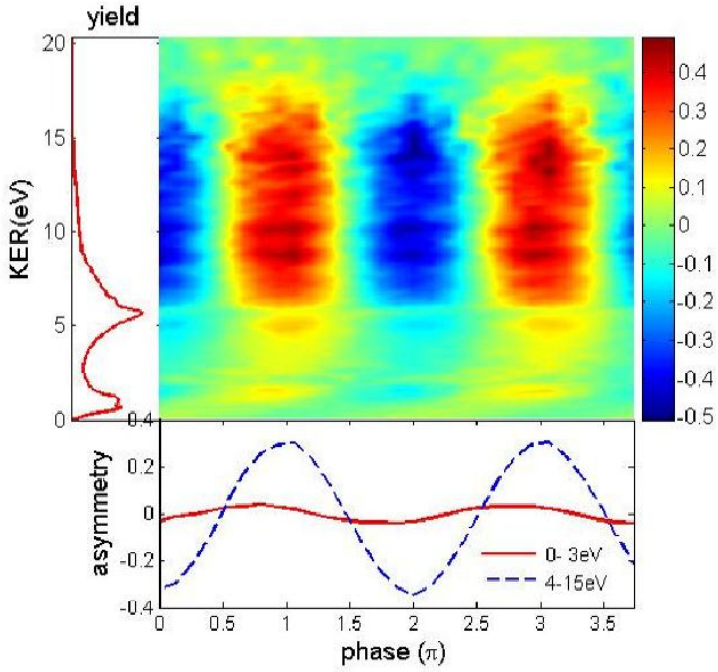

Figure 3.7 Density plot of the asymmetry of the emission of C^+ ions from CO at an intensity of about 2×10^{14} W/cm^2 as a function of KER and two-color phase φ. The upper left panel is a projection of the ion yield versus KER. The bottom panel shows plots of asymmetry versus phase for two chosen energy slices. From Ref. [37].

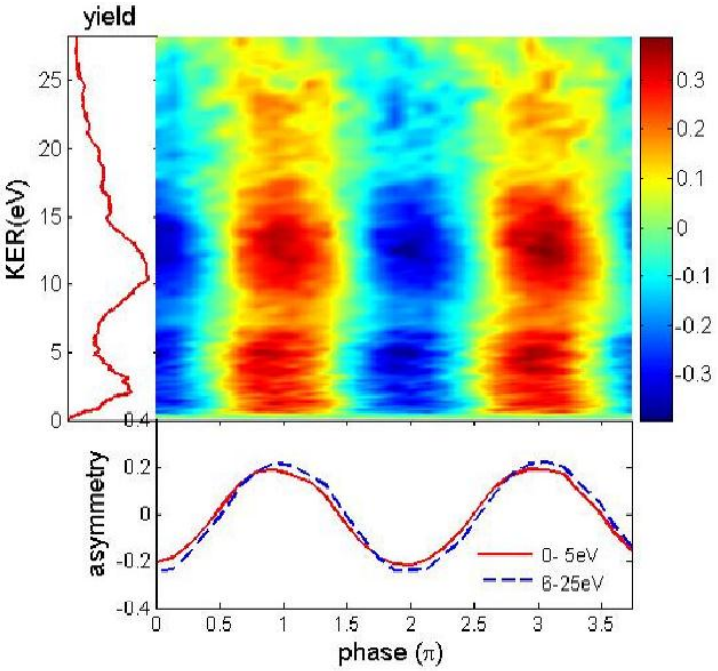

Figure 3.8 Similar to Figure 3.7, but for C^{2+} ions. From Ref. [37].

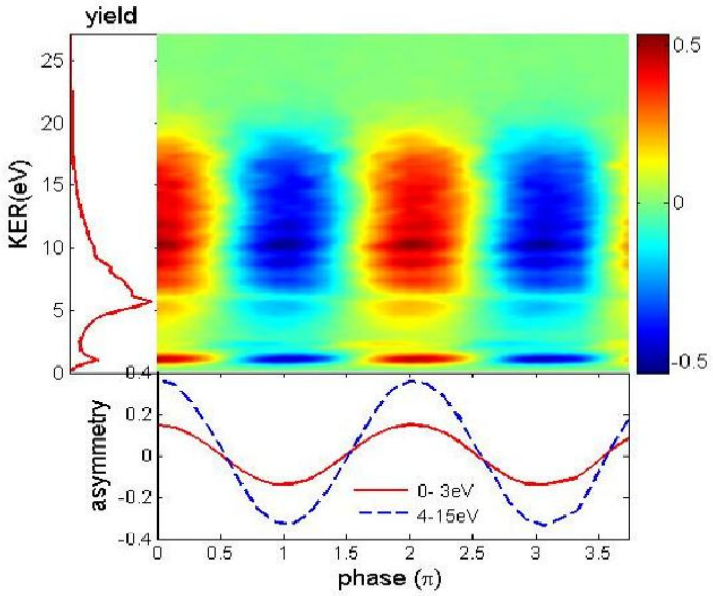

Figure 3.9 Similar to Figure 3.7, but for O^+ ions. From Ref. [37].

Fig. 3.10 shows the evolution of the VMI images for C^+ and O^+ ions from CO under the two-color phase for $\varphi = 0$, $\pi/4$, $\pi/2$, and π.

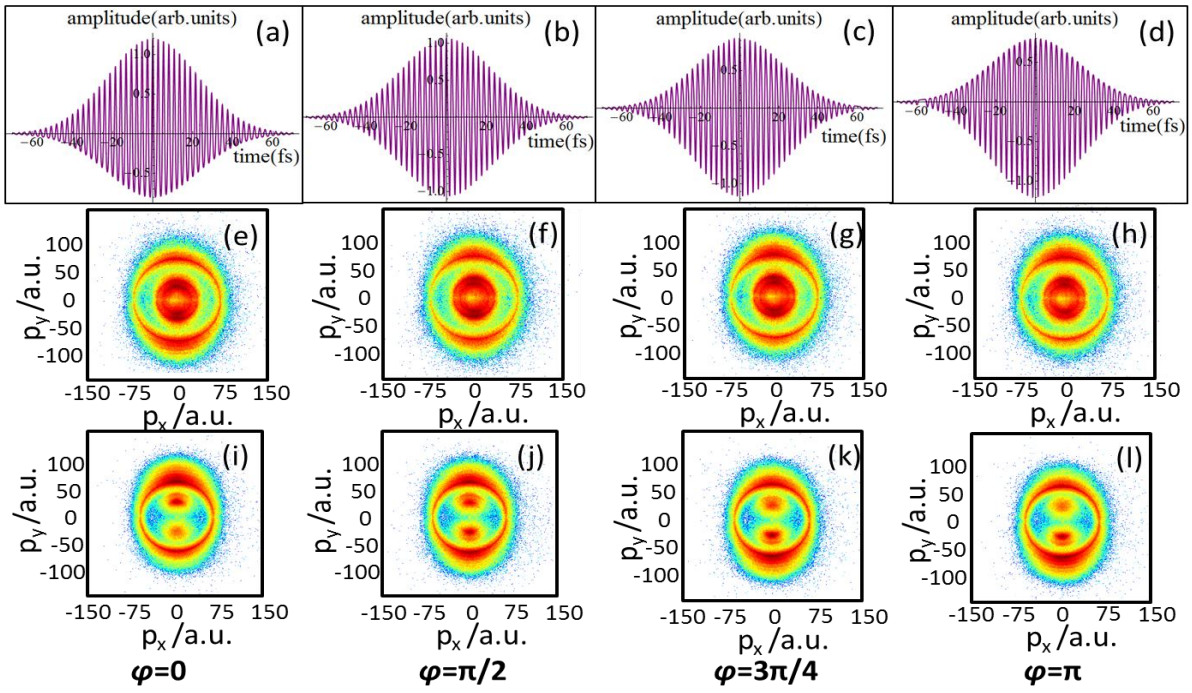

Figure 3.10 The two-color fields and VMI images for C^+ and O^+ ions from CO for different phases. (a-d) Two-color fields for phases φ of 0, $\pi/2$, $3\pi/4$ and π. (e-h) Corresponding raw VMI images for C^+ ions from CO at a laser intensity of about 2×10^{14} W/cm^2. (i-l) Raw VMI images for O^+ ions from CO at a laser intensity of about 2×10^{14} W/cm^2.

Figures 3.11 and 3.12 show asymmetry behaviors for N^+ and O^+ ions from the dissociative ionization of NO in a two-color field. The groups near 2 eV and above 5 eV correspond to dissociation of NO molecules into N^+/O and N^+/O^+, respectively. The asymmetry is clear but much weaker than that for CO. For the O^+ ions from NO, the asymmetry for the KER range of 5 eV to 15 eV has a maximum value of about 0.075. However, the O^+ ions from CO in a similar KER range have a maximum asymmetry value of about 0.4. From the raw VMI images in Fig. 3.13 for the N^+ ions from NO, one can barely see the changes with respect to the two-color phase.

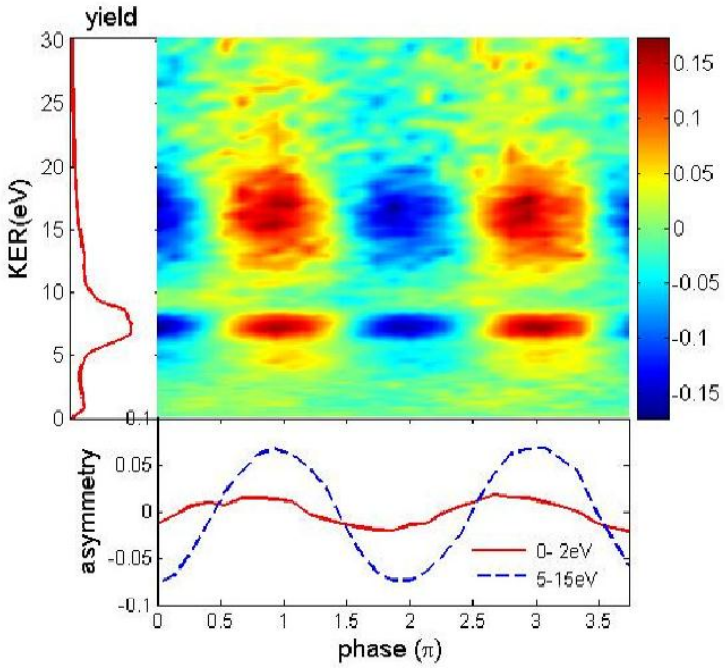

Figure 3.11 Similar to Figure 3.7, but for N^+ ions from NO at an intensity of about 3×10^{14} W/cm^2. From Ref. [37].

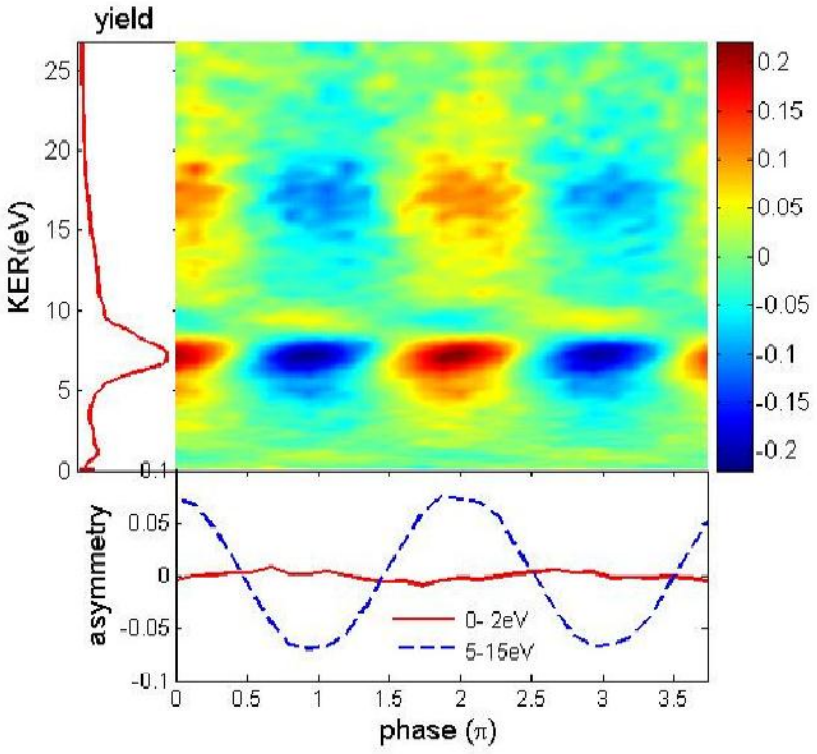

Figure 3.12 Similar to Figure 3.7, but for O^+ ions from NO. From Ref. [37].

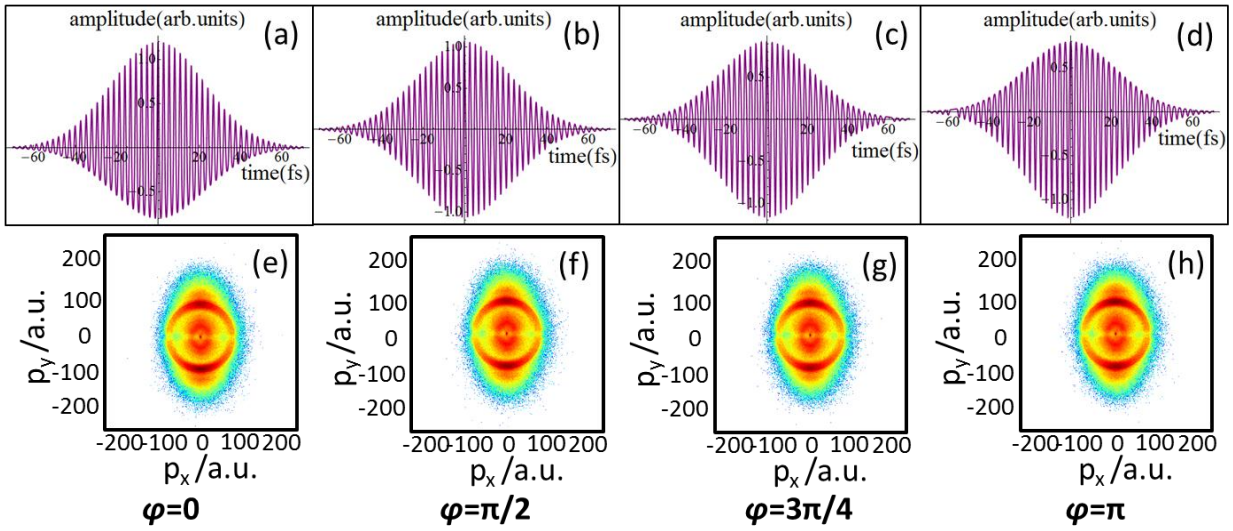

Figure 3.13 The two-color fields and VMI images for N^+ ions from NO for different phases. (a-d) Two-color fields for phases φ of 0, π/2, 3π/4 and π. (e-h) the corresponding raw VMI images for N^+ ions from NO at a laser intensity of about 3×10^{14} W/cm^2.

3.4 Discussion and conclusions

We did not dynamically orient the molecules or pre-select their orientations in our experiment. We irradiate the CO and NO targets with femtosecond two-color laser fields and observe the orientation-dependent ionization. From all the results on the electron and ion emission from CO and NO described in sections 3.2 and 3.3, we arrive at the conclusion that it is easier to ionize the CO and NO molecules when the electric field points from the C or N to the O atom. The asymmetry behavior for CO is much stronger than that for NO. Figures 3.7 and 3.11 show that the asymmetry at zero two-color phase is about 0.3 for CO and 0.07 for NO.

When the diatomic molecules are in an intense laser field, it is well established that the ionization rate depends on the angle between the inter-nuclear axis and the laser polarization direction [40, 46, 61]. A treatment of the ionization rate in this case is given by molecular tunneling theory [40].

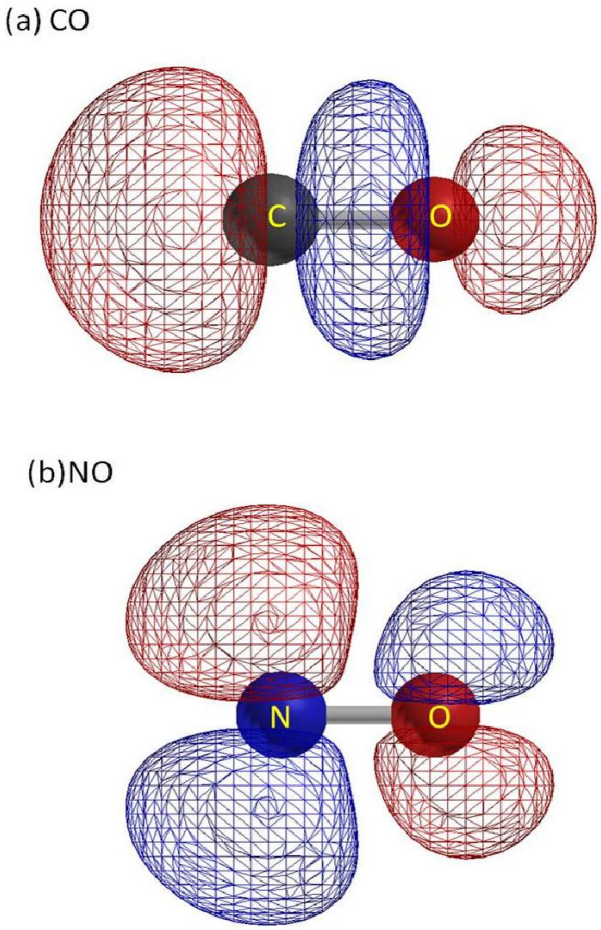

Figure 3.14 Schematic of the HOMOs for (a) CO and (b) NO molecules. From Ref. [37].

The HOMOs for CO and NO molecules are shown in Fig. 3.14. From MO-ADK theory, a higher ionization rate would be expected when the electric field is pointing from the C atom to the O atom in CO [49]. A. T. Lee did calculations on the ionization rates of CO and NO with respect to alignment angles using MO-ADK theory and SFA. The calculated ionization rates for CO and NO as a function of the angle θ between the molecular axis and the electric field are shown in Figures 3.15 and 3.16. The correction for the Stark effect is made by keeping the standard MO-ADK theory or SFA calculations, and using the Stark-shifted ionization potential. In the single-active-electron (SAE) approximation the dipole moment of the HOMO should be used. However, it is better to use the difference $\Delta\mu$ between the dipoles of the molecule and the cation [52, 62]. The $\Delta\mu$ used in our calculations are 1.1 a.u. for CO and 0.28 a.u. for NO, which are obtained from the Gaussian quantum chemistry package [63], with the B3LYP hybrid exchange-correlation functional and Dunning's correlation consistent basis set (AUG-cc-pVTZ). The second order term is found not contributing much to the ionization potentials for both molecules and therefore does not change the ionization rates too much. In Fig. 3.15 (a), the MO-ADK theory calculation without correction predicts a higher ionization rate to occur when the electric field points from the C atom to the O atom. However, when the Stark correction is applied, the result changes its tendency and the higher ionization rate occurs at an opposite direction with the electric field pointing from the O atom to the C atom. In this case, the MO-ADK theory calculation without correction agrees with our experimental results. Fig. 3.15 (b) shows the results of a SFA calculation for CO with and without Stark correction. Here, a short two-color laser pulse with the intensity ratio of 0.09 for the 400 nm and 800 nm components is used. Both results with and without Stark correction show that the higher ionization rate occurs at about 0 degree, corresponding to the electric field pointing from the C to the O atom. These calculations are in agreement with our data.

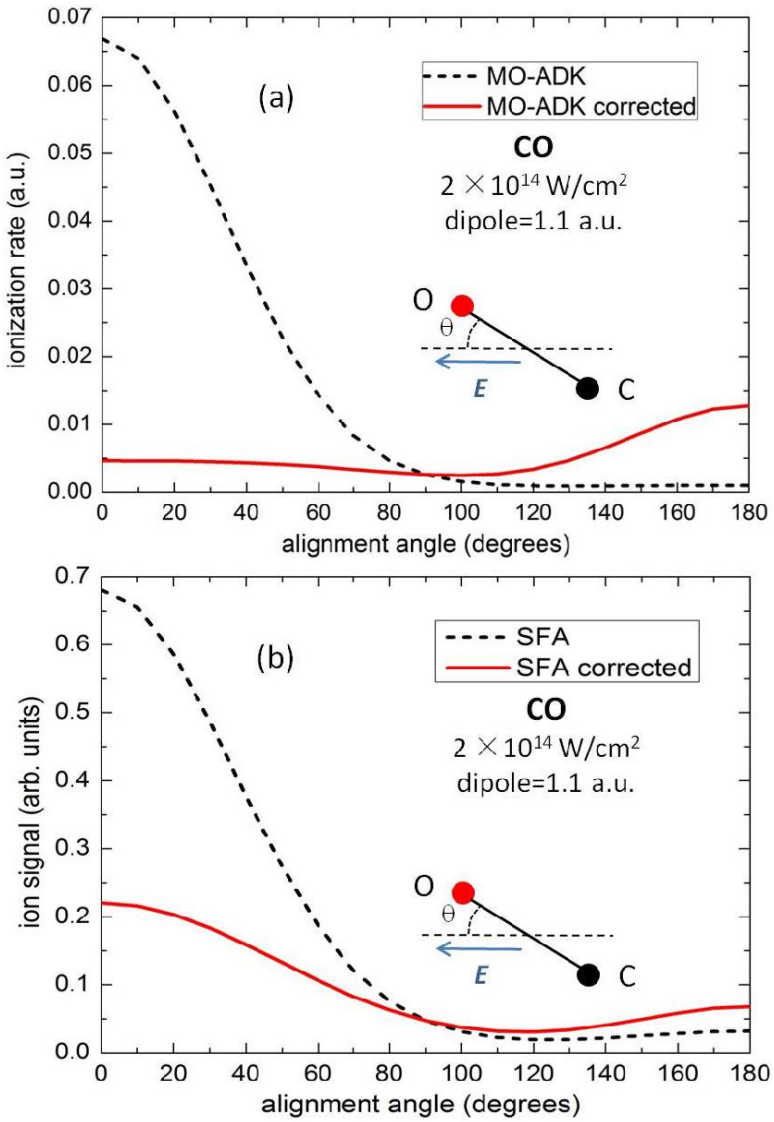

Figure 3.15 Calculated ionization rate of CO as a function of the molecular alignment angle, i.e. the angle θ between the molecular axis and the electric field, as depicted in the subfigures. The electric field pointing from C to O corresponds to $\theta = 0^o$. (a) Calculation from MO-ADK theory with (red solid curve) and without (black dashed curve) correction for the Stark effect. (b) The SFA calculation with (red solid curve) and without (black dashed curve) correction for the Stark effect. From Ref. [37].

Fig. 3.16 shows a similar calculation for NO. In the case of NO, the maximum ionization rate occurs at an angle near 50^o. Both MO-ADK theory and SFA calculations with or without Stark correction predict similar trends. All these calculations are in qualitative agreement with our experimental data.

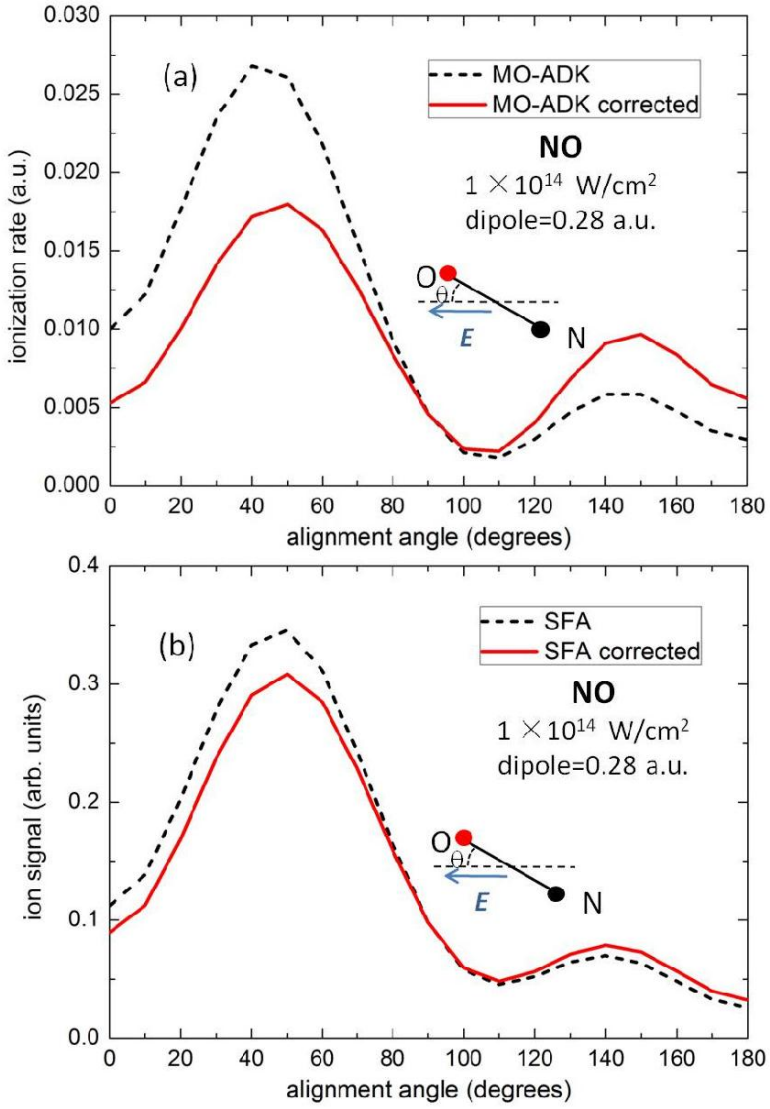

Figure 3.16 Calculated ionization rate of NO as a function of the molecular alignment angle, i.e. the angle θ between the molecular axis and the electric field, as depicted in the subfigures. The electric field pointing from N to O corresponds to $\theta = 0^o$. (a) Calculation from MO-ADK theory with (red solid curve) and without (black dashed curve) correction for the Stark effect. (b) The SFA calculation with (red solid curve) and without (black dashed curve) correction for the Stark effect. From Ref. [37].

The whole situation might be much more complicated than what these calculations can handle. The intensity of the 800 nm component used in the experiments for CO and NO is in the tunneling regime (with a Keldysh parameter γ~0.77 for CO, and γ~0.51 for NO). The second harmonic component is much weaker, which by itself is in the multiphoton regime. Two- or

three- photon processes, as well as resonant excitations are all possible in the ionization and fragmentation process. A full solution of the TDSE including the coupling of many states of the molecules and the molecular ions would be needed. However, we do not have such complex theoretical treatment available at the moment. The full process might not only depend on the removal of the first electron. The group at lower KER range might be substantially contaminated by the extraction of electron from HOMO-1 and HOMO-2, which also have certain angular dependences. Thus it is not reliable to use the lower-KER fragments to track the angular dependence of the ionization of the HOMO. When the HOMO is extracted from the molecule, the molecule is left in a tightly bound state from which fragmentation will not occur. To fragment the molecule, a second step such as rescattering or multiphoton excitation or ionization, which also have angular distributions that may need to be considered. Extraction of the electrons from HOMO-1 or HOMO-2 might leave a highly excited cation, and the fragmentation would be produced easily through bond softening [64]. For the higher-KER fragments, which are from the dication, one can be sure that at least one HOMO electron is removed at a higher probability. However, the removal process of the second electron might also have an angular distribution. The influence of this second step can be ignored for very short pulses and low intensities [35, 41, 42, 49, 50, 57], neither of which are used in our experiment. The influence of the second step is ignored in our treatment, i.e. the angular distribution of the second step is assumed to be isotropic. The calculations in Figures 3.15 (b) and 3.16 (b), the Stark corrected SFA calculation results predict an asymmetry of about 0.75 for CO and 0.5 for NO for a two-color phase $\varphi = 0$. This agrees with the experimental result that the asymmetry for CO is higher than that of NO at zero phase. From Figures 3.7 and 3.11 we can find that the asymmetries at zero two-color phase from experiments are around 0.3 for CO and 0.07 for NO.

To sum up, we measured the asymmetry behavior of ions and electrons from the dissociative ionization of CO and NO in a two-color femtosecond laser field. The results show that the ionization rate is higher for both CO and NO when the electric field points from the C or N to the O atom. This is in agreement with the expectations of MO-ADK theory as well as SFA calculations with Stark corrections. It turns out that the HOMO of small heteronuclear molecules is the dominant factor to determine the favored orientation for ionization in a two-color field.

Chapter 4 - photoionization of C_{60}

This chapter discusses investigations on the ionization of gaseous C_{60} in femtosecond laser fields. Neutral C_{60} molecules are ionized by linearly polarized femtosecond laser pulses at the wavelength of about 800 nm with pulse durations around 30 fs and at the wavelength of about 400 nm with pulse durations around 50 fs. The photoelectron angular distributions (PADs) are measured utilizing a VMI spectrometer. It has been recently reported that for particular photoelectron energies, the angular distribution might originate from the ionization of superatomic molecular orbitals (SAMOs) in C_{60} [1]. It was pointed out that SAMOs arise from the hollow core spherical structures of the C_{60} molecules and differ from Rydberg states by their potential to exhibit electron density inside the fullerene cage. The extracted quantum defects of SAMO do not show typical Rydberg behavior [90]. Up to now, the SAMOs of C_{60} were observed both in solid state fullerene in a scanning tunneling microscopy (STM) experiment [65] and in gas phase neutral C_{60} after excitation by a 120 fs laser field [1]. We get similar results with shorter pulses at the wavelength of 400 nm. Our results with about 30 fs IR laser pulses show a six-lobe angular distribution for low energy electrons, which might come from ionization of a so far unassigned SAMO. This is different from what has been obtained in Ref. [1] by a 120 fs laser field. Furthermore, we performed studies for chirped laser pulses at 800 nm and observe a strong dependence of the photoelectron spectra on chirp, which may be explained by sequential multi-photon ionization via lower lying "doorway" levels [66].

4.1 Review of studies on C_{60} in intense laser fields

C_{60}, also known as buckminsterfullerene, or buckyball, is a spherical molecule consisting of sixty carbon atoms. As is shown in Fig. 4.1, the cage-like structure of C_{60} is made of twenty hexagons and twelve pentagons, which resembles a soccer ball [67]. Theoretical predictions of buckyball molecules appeared in the 1970s [68]. C_{60} was first prepared in the lab in 1985 by Harold Kroto, Robert Curl and Richard Smalley [69], who were awarded the 1996 Nobel Prize in Chemistry for their discovery of C_{60} and the related class of molecules (the fullerenes). C_{60} is a

prototype for studies of complex molecules or clusters. The high order of symmetry makes it easier to build theoretical models, which may then be compared to experimental data.

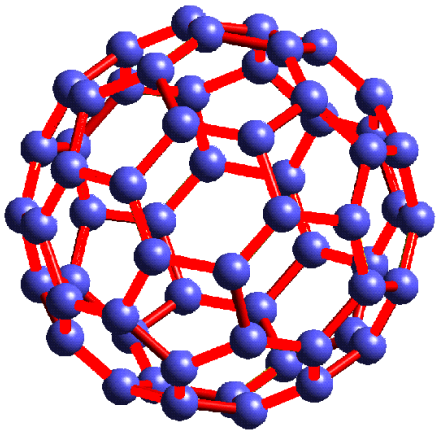

Figure 4.1 Geometric structure of the buckyball molecule C_{60}. From http://www.osti.gov/accomplishments/smalley.html.

For more than a decade, people have been using pulsed lasers to explore the ionization and fragmentation mechanisms of C_{60} [70-73]. The investigation of the ionization behavior of C_{60} using IR pulses with different pulse durations ranging from several picoseconds to tens of femtoseconds shows different results in different time scales [74]. For short pulses with durations below 70 fs, direct multiphoton ionization is predominant [75]. For intermediate pulse durations, the ionization is mainly from the statistical electron emission due to the redistribution of the excitation energy among the electronic degrees of freedom. For pulse durations longer than 500 fs, delayed ionization on timescales as long as microseconds is observed in the mass spectrum [76]. A branch of Rydberg states were discovered in the photoelectron spectra of C_{60} and their dynamics have been explored [77, 78]. The Rydberg series can be nicely predicted by solving the Schrödinger equations using a spherical jellium potential for C_{60} [77].

Strong field excitation and energy redistribution dynamics in fullerene was studied in femtosecond two-color pump probe experiments [66, 78, 79]. Results show that the electron-electron relaxation time in C_{60} is about 100 fs. Furthermore, the LUMO+1 (LUMO stands for lowest unoccupied molecular orbital) is considered to be a "doorway" state in a non-adiabatic multielectron excitation process, as is shown in Fig. 4.2. When inspecting the photoelectron energy spectra for C_{60}, a series of peaks can be seen superimposed on the thermal electron signal. The thermal electron signal might come from thermionic emission, where the distribution of

thermal electrons can be approximated by an exponential function $I(\varepsilon) \propto \exp(-\varepsilon / k_B T)$, with ε being the electron kinetic energy and T the effective electron temperature [90]. With the help of angular resolved photoelectron detection technique, the PADs of C_{60} were studied and anisotropic thermal electron emission with respect to the laser polarization was found [80, 81]. Recently, solid state C_{60} on a Cu surface measured under STM shows that C_{60} exhibits hydrogen-like SAMOs [65], as shown in Fig. 4.3. Recently, SAMOs were also found to play a role in the photoionization of gas phase C_{60} in a 120 fs laser field [1]. For Rydberg states, the orbital of electron is far from the parent core and the electron only feel the screening of all the other electrons as a point charge. For the SAMOs, electron density can also exist inside the fullerene cage.

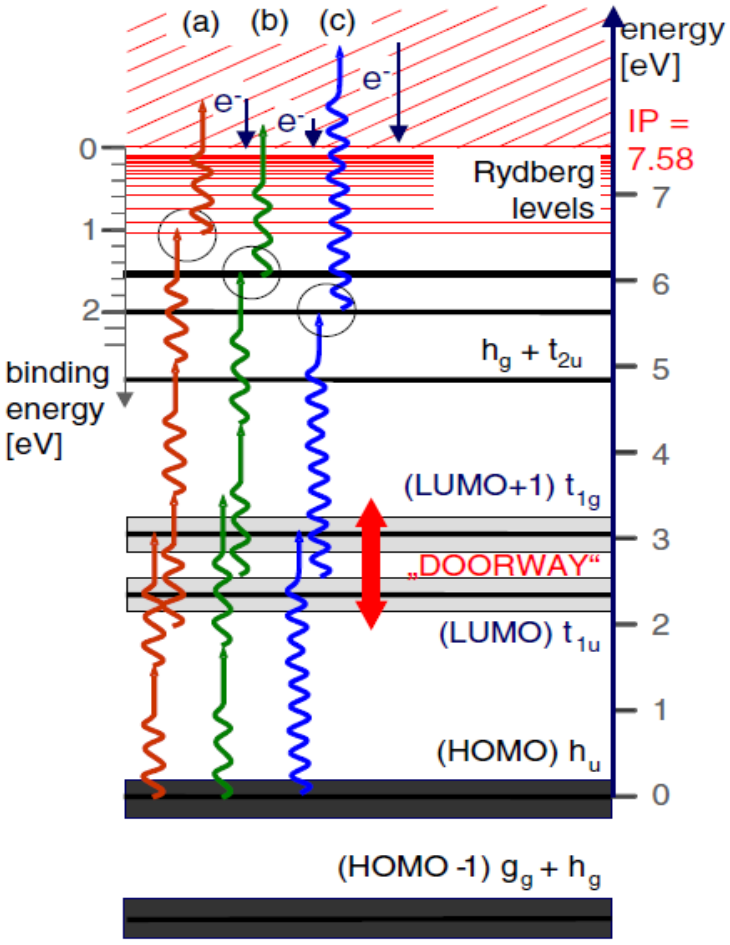

Figure 4.2 Energy level diagram for C_{60}. From Ref. [78].

If there is coexistence of Rydberg states and SAMOs in C_{60}, it would be interesting to find out their relative importance in photoionization in intense fields. The laser parameters that may play a role are the intensity, pulse duration, wavelength, chirp etc.

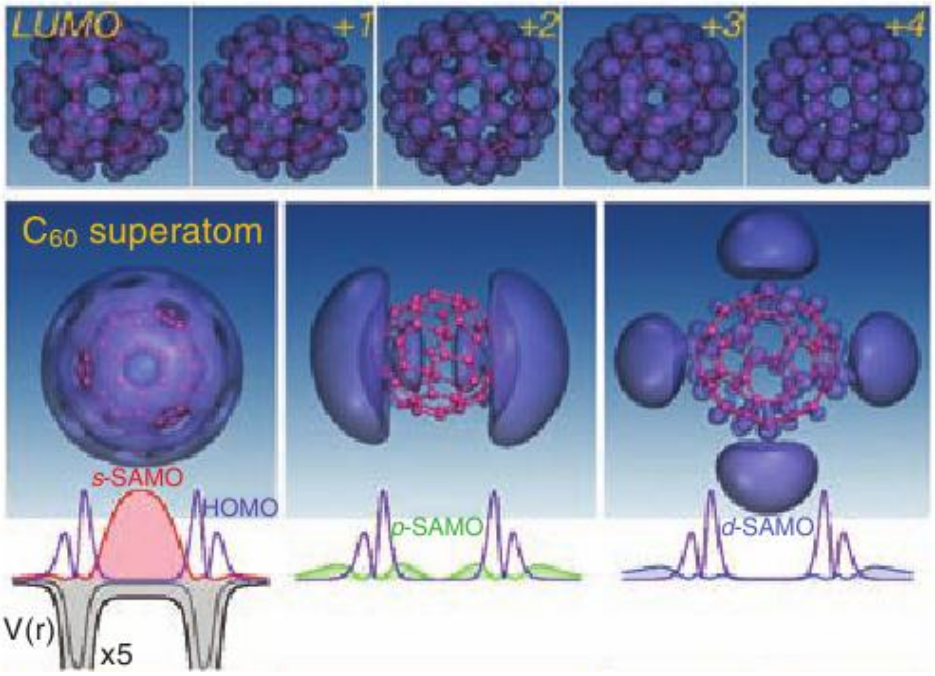

Figure 4.3 C_{60} molecular orbitals. From Ref. [65].

4.2 Ionization of C_{60} by a femtosecond laser

When C_{60} is excited by intense laser field, ionization and fragmentation will occur depending on the laser intensity and the pulse duration. In our study, moderate laser intensities (in the order of 10^{12} W/cm^2 to 10^{13} W/cm^2) are used. For single ionization of C_{60}, characteristic PADs below kinetic energies for one photon emission are found in the photoelectron images. At higher intensities, multiple ionization of C_{60} occurs. A typical ion time of flight (TOF) spectrum obtained in the photoionization of C_{60} is shown in Fig. 4.4. Several peaks appear in the TOF spectrum, such as C_{60}^+ and C_{60}^{2+}. We systematically measured the ion yields of C_{60}^+ and C_{60}^{2+} under different laser intensities with 35 fs pulses at 800 nm, see Fig. 4.5. When the laser intensity goes below 5×10^{12} W/cm^2 for a 35 fs pulse, there is no signal from any other ions except for C_{60}^+. A six-lobe PAD appears for the electrons with low kinetic energies when the intensity is adjusted such that there is only C_{60}^+ in the TOF measurement.

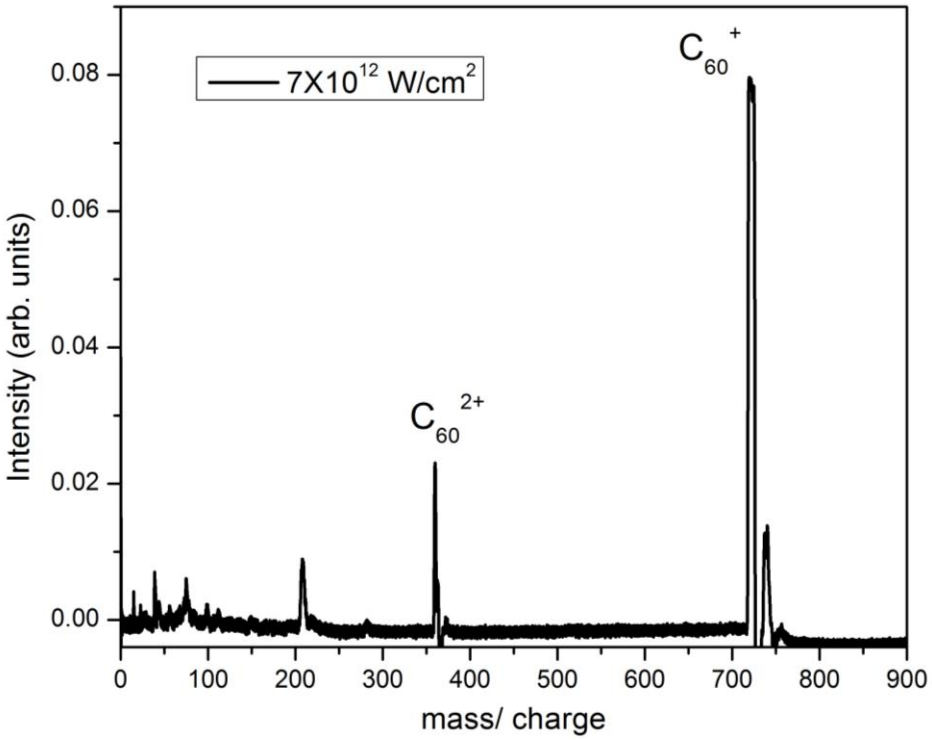

Figure 4.4 Ion TOF spectrum of C_{60} when excited with 35 fs pulses at 800 nm, with an intensity of 7×10^{12} W/cm^2. The peak of C_{60}^{+} and C_{60}^{2+} ions are pointed out in this figure.

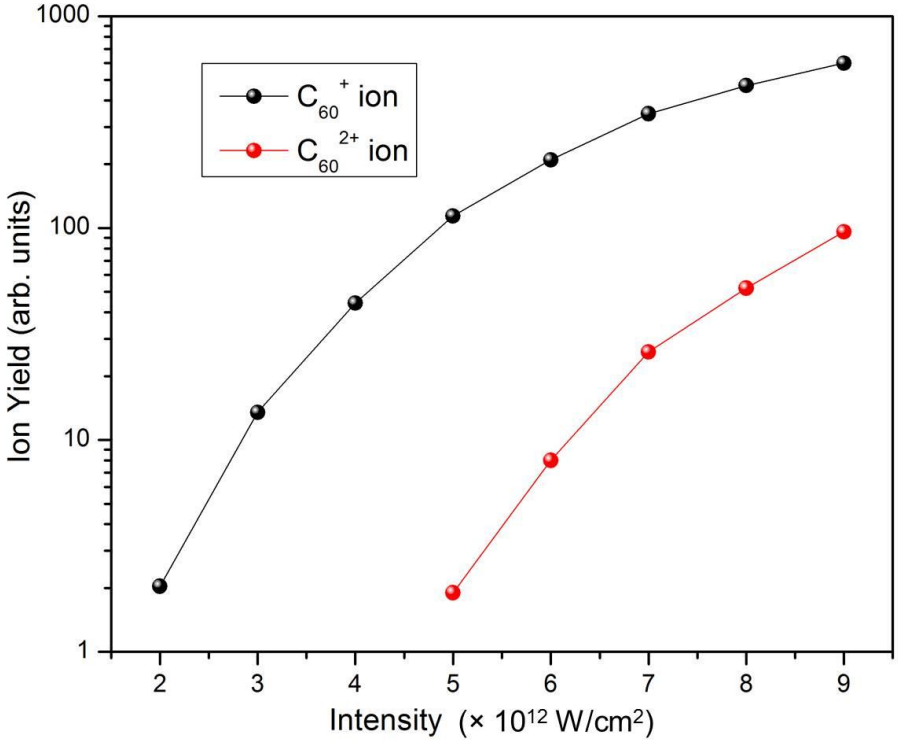

Figure 4.5 Yields of C_{60}^{+} and C_{60}^{2+} ions versus laser intensity for a 35 fs laser field.

4.2.1 Photoionization with femtosecond near-infrared laser pulses

The experimental setup for this part is briefly discussed in section 2.3. A beam of linearly polarized, near-infrared laser pulses with pulse durations around 30 fs is focused onto a neutral C_{60} beam generated from a homemade oven. To obtain a photoionization signal with enough statistics at low laser intensities, the oven is maintained at about 500^{o}C. Some inverted photoelectron VMI images for C_{60} using both PULSAR and KLS as laser sources are shown in Figures 4.6 and 4.7, respectively. The experiments have been carried out with both laser systems to check the reproducibility. The new laser system PULSAR offers a 5-time higher repetition rate than KLS, which motivated the use of PULSAR for shorter acquisition times and increased statistics. KLS has a pulse duration of about 35 fs measured with a FROG device [89] that was home-built by Chang's group. PULSAR has a pulse duration of about 27 fs measured with the FEMTOMETER^{TM} interferometric autocorrelator (FEMTOLASERS). The intensities are obtained by first principles, which are based on the Gaussian beam calculation from the laser power, pulse duration and the far-field laser profile, and then compared with measurements of the cutoff of Xe ATI spectra at high intensity. A neutral density filter is applied to change the intensity in the experiments. The images from KLS have more fine structures, which might arise from the slightly longer pulse durations and also from the difference between the central wavelengths of the two laser system, which are 785 nm for KLS and 790 nm for PULSAR. For both the results from PULSAR and from KLS, a six-lobe structure shows up in the low electron energy region for low laser intensities.

Photoelectron spectra in both energy and angle can provide a lot of information on the electron dynamics in intense laser field [15, 91]. For an ATI experiment, if long pulses (the duration of the laser pulse is longer than the time for a photoelectron to leave the interaction volume) are used to ionize the target, the detected electron kinetic energies will not change with laser intensity. This is due to the fact that the increased ionization potential of the parent core is almost equal to the kinetic energy gained by the electron from ponderomotive acceleration. However, for short pulses with sub-picosecond durations, the electron kinetic energies are intensity dependent. During the laser pulse, the ionization potential is increased by an amount of the ponderomotive energy Up, but there is no time for the electron to accelerate before the pulse leaves. As a result of this, the electron kinetic energy will be reduced by Up. The real

photoelectron energies as well as the angular distributions when ionization takes place can be detected. The angular distribution of electron might also originate from diffraction. The fine structures observed in the ATI groups for femtosecond pulses are attributed to Freeman resonance. The weakly bound excited states as well as the ionization potential all shift upward by about Up, thus these levels will become resonance with a certain number of photon energy at some intensity (Up is proportional to laser intensity), resulting in a resonant enhancement. When using femtosecond intense laser pulses, there are two different regions of interest depending on the laser intensity. If the Keldysh parameter γ>>1, multiphoton process is predominant, leading to ATI structures in the photoelectron energy spectra (PES). In this region, the PES as well as the angular distributions often include complex structures from Freeman resonances. If γ<1, it is in the tunneling region. The resonant structures reflecting the atomic/molecular structure of the target are not expecting.

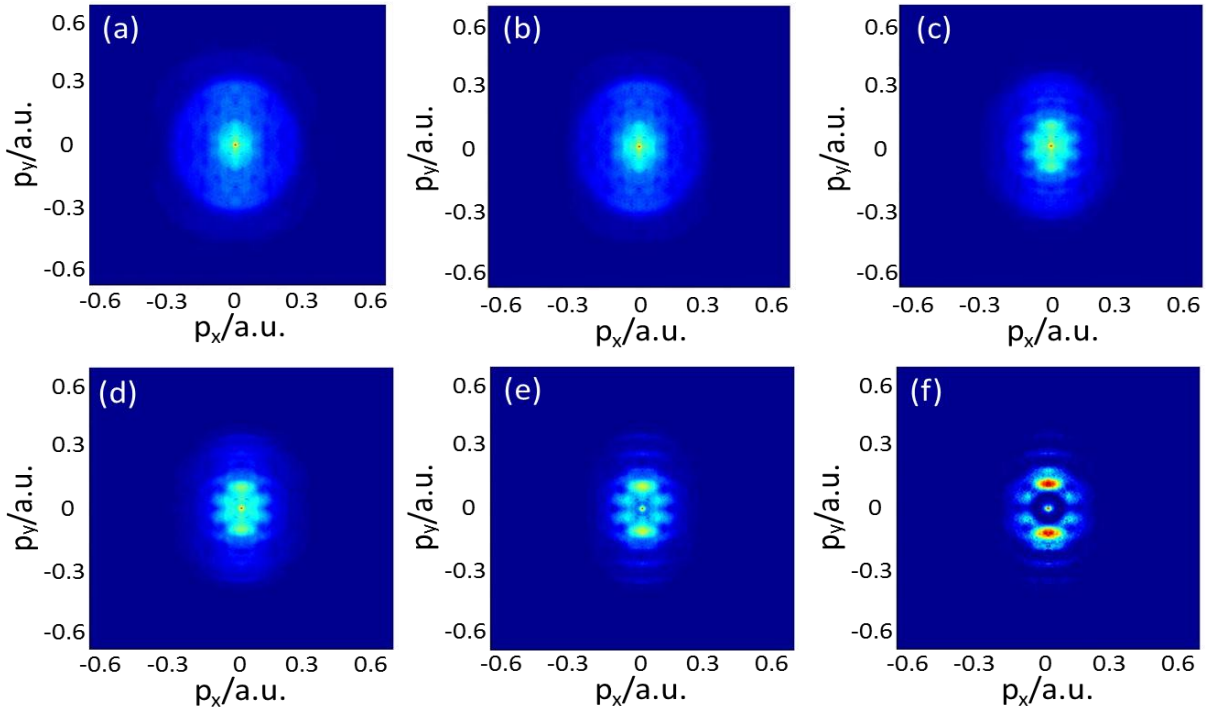

Figure 4.6 Inverted photoelectron VMI images of C_{60} under excitation of 785 nm, 27 fs laser pulses (PULSAR) with different laser intensities. (a) 2.0×10^{13} W/cm^2; (b) 1.5×10^{13} W/cm^2; (c) 1.0×10^{13} W/cm^2; (d) 7.5×10^{12} W/cm^2; (e) 5.0×10^{12} W/cm^2; (f) 3.0×10^{12} W/cm^2.

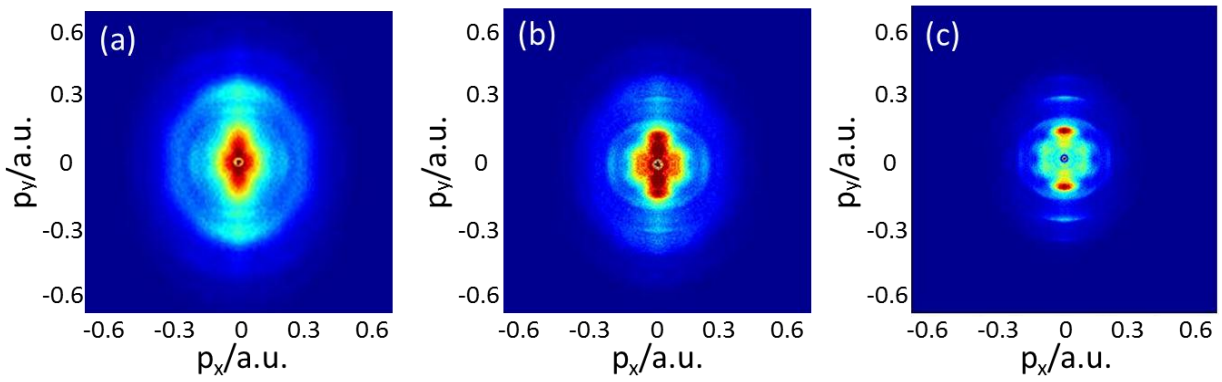

Figure 4.7 Inverted photoelectron VMI images of C_{60} under excitation of 790 nm, 35 fs laser pulses (KLS) with different laser intensities. (a) 6.0×10^{12} W/cm^2; (b) 3.6×10^{12} W/cm^2; (c) 2.4×10^{12} W/cm^2.

The photoelectron energy spectra for C_{60} are shown in Figures 4.8 (PULSAR) and 4.9 (KLS). These spectra are obtained by integrating over an angular range of 20 ^{o} along the laser polarization direction (y-direction). The inserted subfigure in Fig. 4.8 shows a comparison of the photoelectron energy spectra with respect to the integration angle range at a laser intensity of about 5.0×10^{12} W/cm^2. The spectrum is noisier for a smaller angle range. For a larger integration cone, the spectrum is smoothed out. Thus we choose a moderate range of 20^{o} for our data analysis. The spectra for the same laser intensity look generally similar for both PULSAR and KLS. There is a small energy shift between these two groups of data, which might come from the central wavelength difference between the two laser systems. From Figures 4.8 and 4.9, we can see that for lower intensities, there are several apparent peaks lying around 0.2 eV, 0.9 eV, and 1.7 eV. Comparing with the data reported in Ref [81], the thermal electron emission, which shows as an isotropic electron emission with an exponential decay versus electron energy, is highly suppressed in our case by the use of shorter pulses.

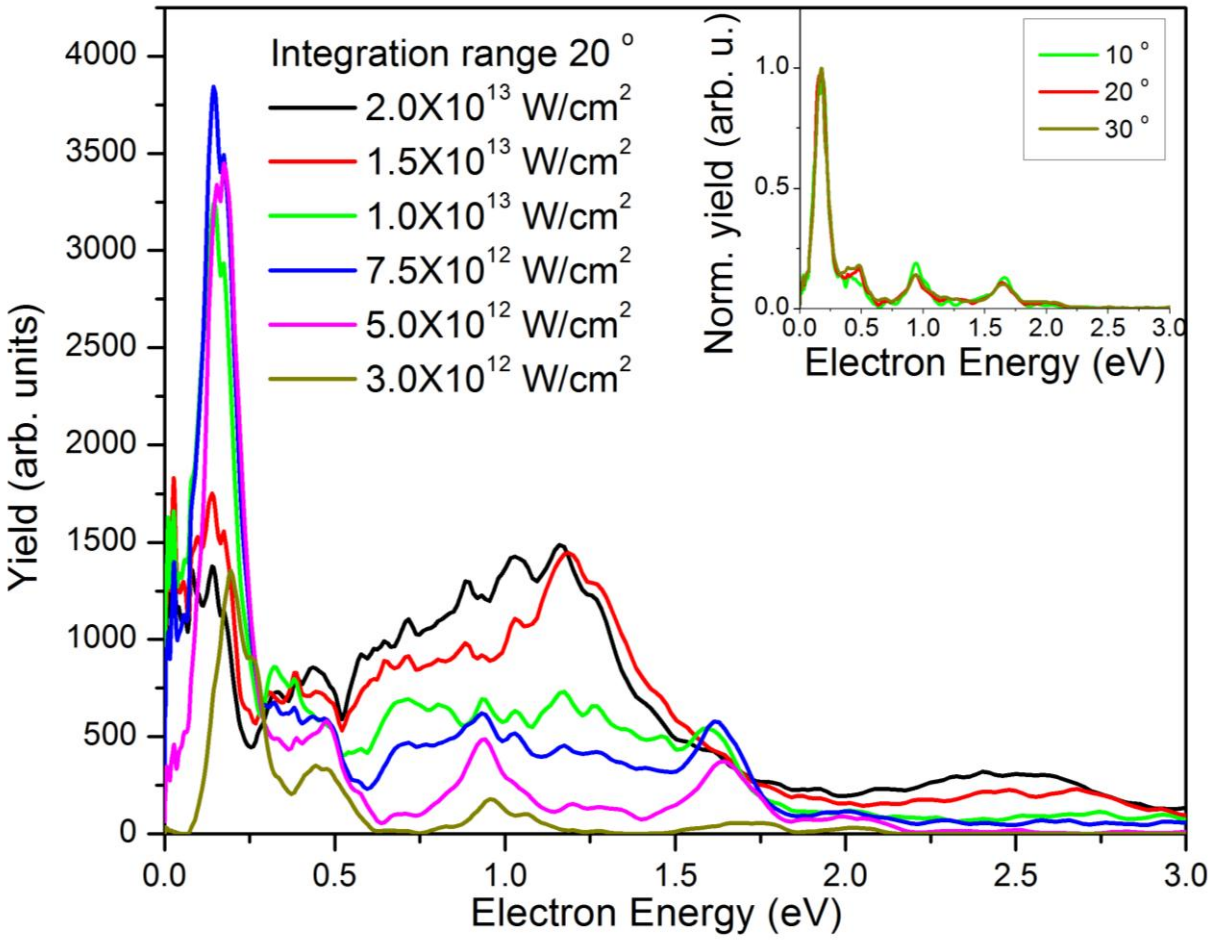

Figure 4.8 Photoelectron spectra for different laser intensities using the PULSAR laser. Inserted figure: Comparison of the photoelectron energy spectra with different integration angle ranges at an intensity of 5.0×10^{12} W/cm^2. The spectra are normalized to the highest peak around 0.2 eV.

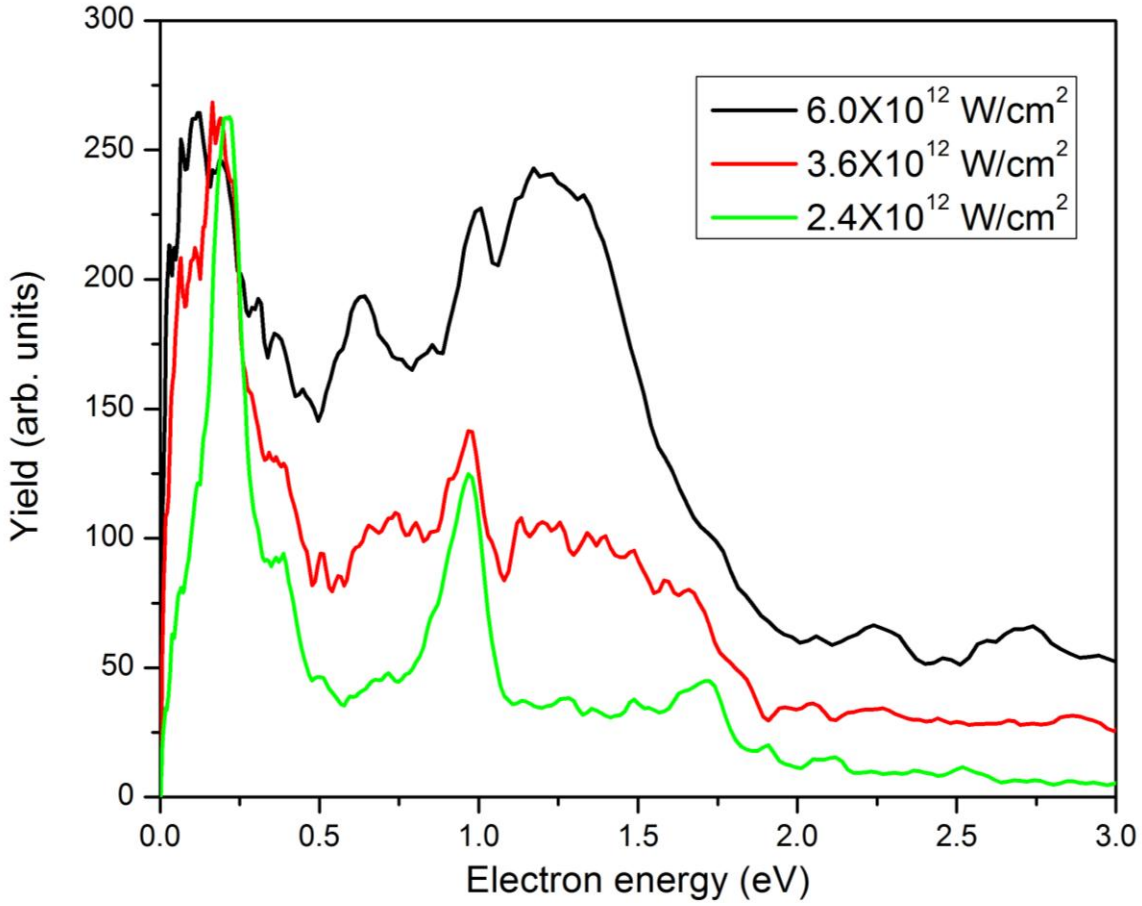

Figure 4.9 Photoelectron spectra from C_{60} for different laser intensities using KLS.

The PADs of the data shown in Fig. 4.6 (e) at the intensity of 5.0×10^{12} W/cm^2 are further analyzed to illuminate photoionization property of C_{60} in this condition. For this purpose, the PADs of different electron energy regions (indicated in Fig. 4.10) are fitted with Legendre polynomials given in equation (4.1).

$$I(\theta) = \beta_0 \times [1 + \beta_2 \times P_2(\cos\theta) + \beta_4 \times P_4(\cos\theta) + \beta_6 \times P_6(\cos\theta) + \beta_8 \times P_8(\cos\theta)]. \quad (4.1)$$

Here, β_0, β_2, β_4, β_6 and β_8 are the fitting parameters, where β_0 is the total differential cross section σ divided by 4π, β_2 to β_8 are the anisotropy parameters which determine the PAD shape. θ is the angle between the direction into which the electron is ejected with respect to the laser polarization direction. P_n ($\cos\theta$) is the n-th order Legendre polynomial. The fitting is performed using Origin version 8.1. The results of the fitting are shown in Fig. 4.11 with the parameters contained in Table 4.1.

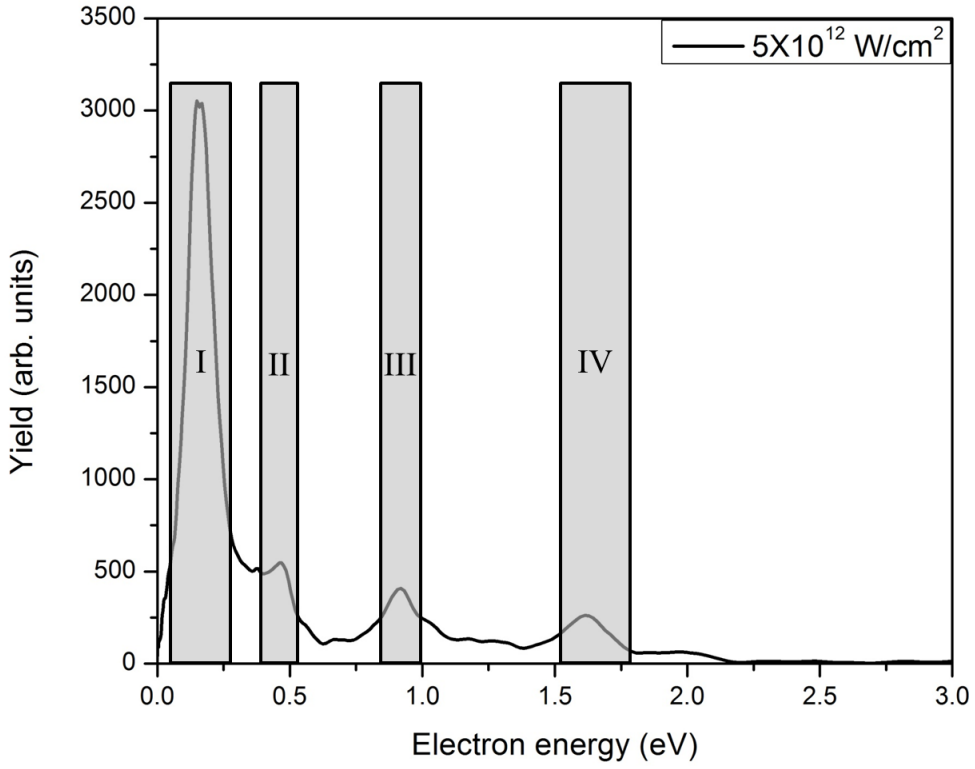

Figure 4.10 Photoelectron spectrum at 5.0×10^{12} W/cm^2, obtained with PULSAR. The shadowed areas are the regions used in the analysis of the angular distributions. In Ref. [1], Peak I is assigned to the ionization from a p-SAMO; Peak III is assigned to the ionization from an s-SAMO.

	Energy range (eV)	β_0	β_2	β_4	β_6	β_8
I	0.08-0.30	114.8 ± 0.9	0.97 ± 0.02	0.67 ± 0.02	1.19 ± 0.03	-0.10 ± 0.02
II	0.44-0.55	5.9 ± 0.1	1.00 ± 0.04	0.28 ± 0.05	0.29 ± 0.05	0.13 ± 0.05
III	0.87-1.01	1.64 ± 0.05	1.75 ± 0.09	1.4 ± 0.1	1.3 ± 0.1	1.1 ± 0.1
IV	1.55-1.79	0.83 ± 0.03	2.2 ± 0.1	1.7 ± 0.1	1.9 ± 0.1	1.4 ± 0.1

Table 4.1 Parameters obtained from the fitting of the PADs for regions I to IV shown in Fig. 4.10 to Legendre polynomials. In Ref. [1], Peak I is assigned to the ionization from a p-SAMO; Peak III is assigned to the ionization from an s-SAMO.

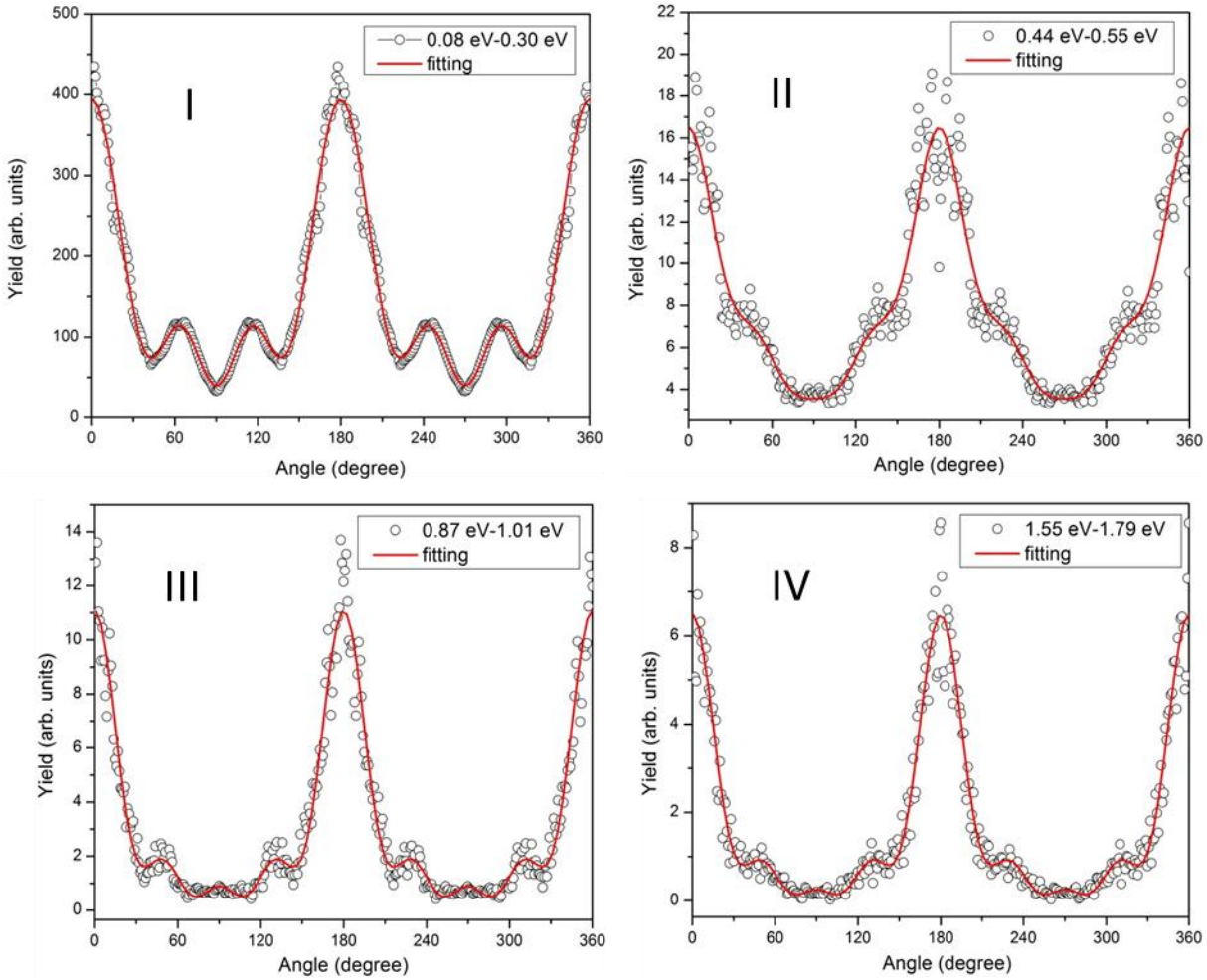

Figure 4.11 PADs and fitting results for different electron energy regions. The black hollow circles are the experimental data; the red curves are the fitting results according to equation (4.1).

The most interesting angular distribution occurs in region I, in the electron energy range from 0.08 eV to 0.30 eV. This corresponds to the six-lobe structure near the center in Fig. 4.6 (e). In Ref. [1], the peak in the electron energy spectrum in this region is assigned to ionization from a p-SAMO. The analysis is based on time-dependent density functional theory (TD-DFT) calculations and on an analysis of the β_2 parameter as a function of photoelectron kinetic energy for different excitation wavelength (which we have not investigated in our studies). We cannot compare the excitation energy dependent β_2 parameters, but we can evaluate the β_2 parameter for our laser wavelength (785 nm). Our results differ from the parameter reported in the literature for 120 fs pulses [1]. Our fitting results with equation (4.1) result in a β_2 parameter around 0.97 ±

0.02 for Peak I, the β_2 parameter for the same energy region reported in Ref. [1] was around -0.6. Furthermore, in Ref. [1] the peak near 0.7 eV is assigned to the ionization from an s-SAMO. The corresponding peak in our data is located near 0.9 eV (peak III), where the small shift originates from the shift in excitation photon energy between the two studies.

It should be noted, that Campbell and coworkers fitted their results to equation (4.2) below, which represents the PAD of one-photon ionization from an isotropic target by a linearly polarized light [82]

$$I(\theta) = \frac{\sigma}{4\pi}[1 + \beta \times \mathrm{P}_2(\cos\theta)]. \qquad (4.2)$$

It is obvious from the data shown in Figs. 4.6, 4.7 and 4.11 that this formula would not provide a suitable fit of our data between 0.08 eV to 0.30 eV since the images show multi-lobe angular distributions. In fact, our fitting results using equation (4.1) show that multiphoton ionization or the population of certain resonant state with defined orbital might play a significant role in the photoelectron emission.

It is possible that the ionization has a selection on either molecules with certain orientations or whose electronic orbital angular momentum vectors have constrained directions in space. A more general expression for PADs is given by [28]

$$I(\theta,\phi) \propto \sum_{L=0}^{2n+2m} \sum_{M=-L}^{L} \beta_{L,M} Y_L^M(\theta,\phi). \qquad (4.3)$$

Here, n is the number of photons needed for excitation, m is the number of photons needed for ionization. L is the orbital angular momentum quantum number; M is the magnetic momentum quantum number. $Y_L^M(\theta, \phi)$ is the spherical harmonic function. For an N-photon process, equation (4.3) can be simplified to

$$I(\theta) = \sum_{n=0}^{N} \beta_{2n} P_{2n}(\cos\theta). \qquad (4.4)$$

Since the ionization potential for C_{60} is 7.58 eV [83], at least five IR photons are needed to get to the continuum. It is also probable that the electron is excited to populate certain states which resemble well defined orbitals, and then ionized by an extra photon.

Without further studies, it remains unclear, why the photoionization with shorter laser pulses in the near-infrared shows different PADs as compared with the results obtained in a 120

fs laser field. Further investigations as a function of pulse duration and/or using two-color pump probe schemes are needed.

4.2.2 Photoionization with second harmonic UV pulses

Similar experiments have been carried out in the UV. The UV pulses are generated by frequency doubling the near-infrared beam via a BBO crystal with a thickness of 200 μm. The second harmonic component is separated after the BBO by two dichroic mirrors. Inverted VMI images for photoelectrons from C_{60} in intense UV laser fields are shown in Figures 4.12 and 4.13. The duration of the UV pulses is estimated to be around 50 fs. The images and PADs obtained from KLS and PULSAR are similar to what is reported in Ref. [1].

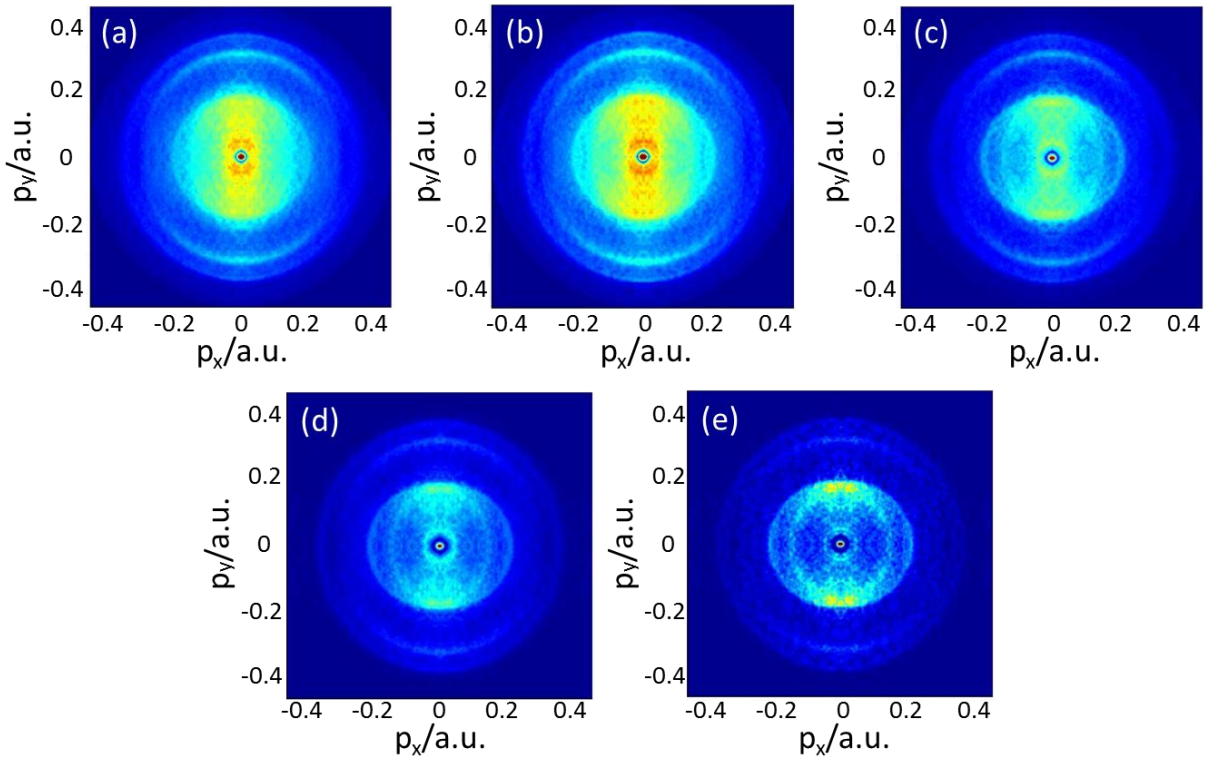

Figure 4.12 Inverted photoelectron VMI images of C_{60} under excitation of 395 nm, 50 fs laser pulses (KLS) with different laser intensities. (a) 2.0×10^{13} W/cm^2; (b) 1.5×10^{13} W/cm^2; (c) 1.0×10^{13} W/cm^2; (d) 7.5×10^{12} W/cm^2; (e) 5.0×10^{12} W/cm^2.

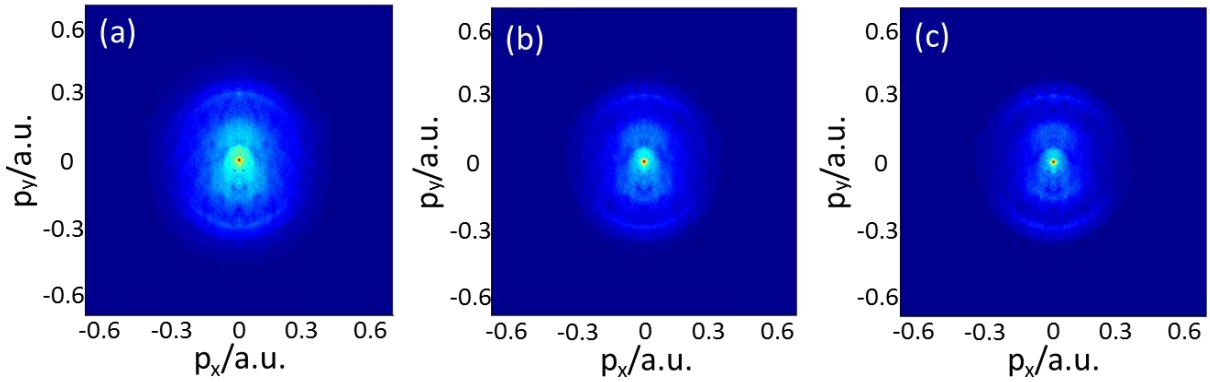

Figure 4.13 Inverted photoelectron VMI images of C_{60} under excitation of 393 nm, 45 fs laser pulses (PULSAR) with different laser intensities. (a) 6.0×10^{12} W/cm^2; (b) 4.0×10^{12} W/cm^2; (c) 2.0×10^{12} W/cm^2.

The corresponding photoelectron spectra are shown in Figure 4.14. These spectra agree with those reported in Ref. [1] to some extent. However, the spectra in the reference are modified by subtracting thermal electron signals. The shorter pulse duration in our study and an anisotropic thermal background do not permit to easily subtract such contributions from our data. In Ref. [1], the peak around 1.6 eV electron energy is assigned to a p-SAMO with a β_2 parameter of about 1.5. Our fitting results with the same formula result in a β_2 parameter around 1.2, which significantly decreases with laser intensity, as is shown in Table 4.2. The effect might be attributed to a background of thermal electrons, leading to a more isotropic angular distribution. Further studies as a function of pulse duration and intensity would be needed to evaluate this aspect in detail.

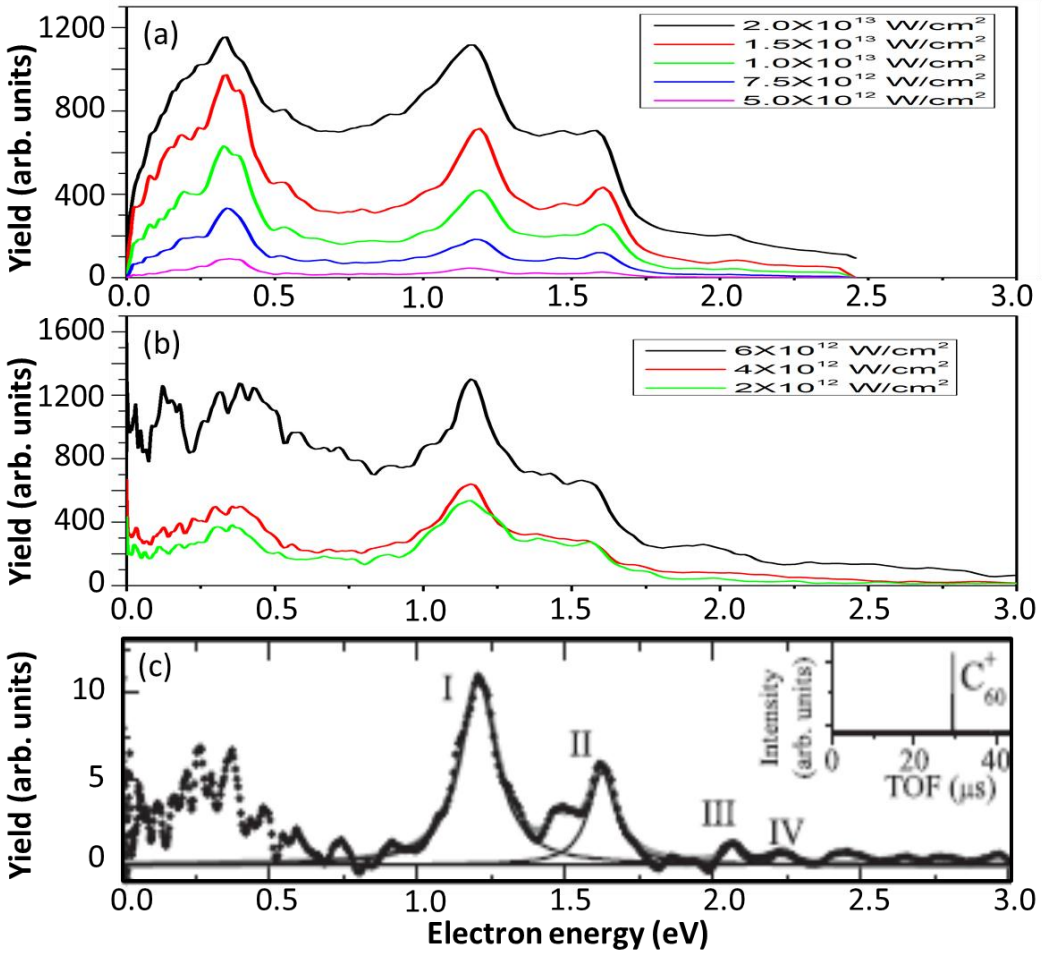

Figure 4.14 Photoelectron spectra under different laser intensities at the wavelength of 400 nm getting from (a) KLS and (b) PULSAR. (c) Photoelectron spectra of C_{60} with 400 nm, 120 fs laser pulses of intensity 3.0×10^{11} W/cm^2, modified from Ref. [1].

Intensity ($\times10^{12}$W/cm^2)	2	4	5	6	7.5	10	15	20
β_2	1.19	1.09	0.74	0.97	0.77	0.77	0.70	0.64
Standard error	0.04	0.03	0.03	0.02	0.02	0.02	0.02	0.01

Table 4.2 Fitting results of β_2 based on Eqn. 4.2 under different laser intensities for the PAD obtained for the energy region near 1.6 eV.

4.3 Studies on the photoionization of C_{60} as a function of chirp

The dependence of the PADs as well as the photoelectron spectra for C_{60} on the laser pulse chirp was studied and is discussed in this section. Linear chirped pulses are obtained by tuning the grating spacing inside the laser compressor. The corresponding chirp is obtained from a first principle calculation using the grating parameters according to

$$GDD = -\frac{\lambda^3 L}{\pi c^2 d^2}\left(1-\left(\frac{\lambda}{d}-\sin\theta\right)\right)^{-3/2}. \quad (4.4)$$

Here, GDD is the group delay dispersion (in fs^2) of the grating pair. λ is the central wavelength. L is the center to center separation of the gratings, which is about 320 mm. d is the groove period 1/1200 mm. θ is the incidence angle to the grating normal, which is 38^o. Once we get the GDDs, we can estimate the durations of the chirped pulses. In our experimental condition, the pulse is stretched from 27 fs to about 60 fs for the maximum chirp that we introduced (± 295 fs^2).

We chose a laser intensity of 5.0×10^{12} W/cm^2. At this intensity, ionization of C_{60} is limited to the creation of the cation and in the near-infrared the six-lobe structure is observed. The peak intensity is maintained when changing the chirp by adjusting the pulse energy such that the photoelectron yield remains constant. The inverted photoelectron VMI images for chirped pulses are shown in Fig. 4.15. The corresponding inverted VMI image from the Fourier transform-limited (FTL) pulse was shown in Fig. 4.6 (e). It can be seen, that the PADs with positively chirped pulses are modified more strongly than those for negatively chirped pulses. In both cases, a broadening of the features at higher electron momenta (>0.1 a.u.) can be observed.

The PADs over different electron energy regions are fitted to equation (4.1). For the electrons in the energy range from 0.1 eV to 0.2 eV (or in the momenta range from 0.09 a.u. to 0.12 a.u.), corresponding to the inner six-lobe structure, the fitting curves as well as the parameters obtained for different chirps are shown in Fig. 4.16. It is noticed from the plot that the parameters β_2, β_4 and β_6 decrease with increasing chirp for the positive chirps. No clear tendencies with chirp are found for other peaks in the spectra.

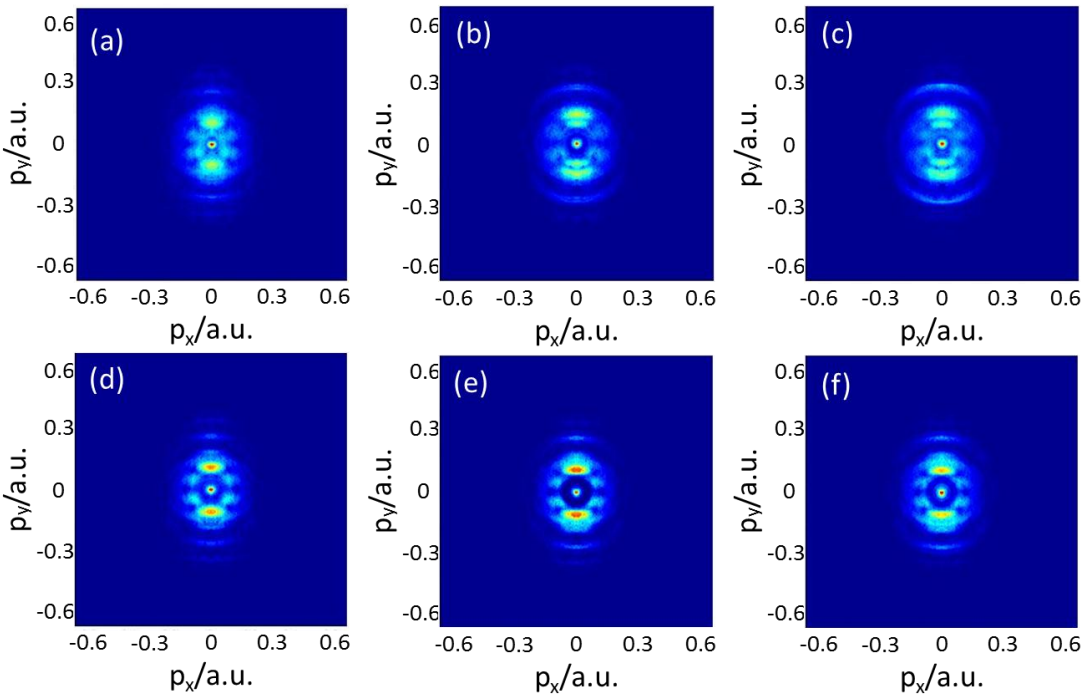

Figure 4.15 Inverted photoelectron VMI images of C_{60} under excitation of chirped laser pulses (PULSAR) at the laser intensity of 5.0×10^{12} W/cm^2. (a) +55 fs^2; (b) +175 fs^2; (c) +295 fs^2; (d) -55 fs^2; (e) -175 fs^2; (f) -295 fs^2.

The photoelectron spectra for positively and negatively chirped pulses obtained from the full angular integration of the VMI images are depicted in Fig. 4.17. It can be seen in Fig. 4.17 that the spectrum profiles are modulated for the chirped pulses. Several new peaks appear (such as the peaks around 0.3 eV and 1.2 eV) and evolve with the chirp. The ratio of these new peaks is different for positively and negatively chirped pulses.

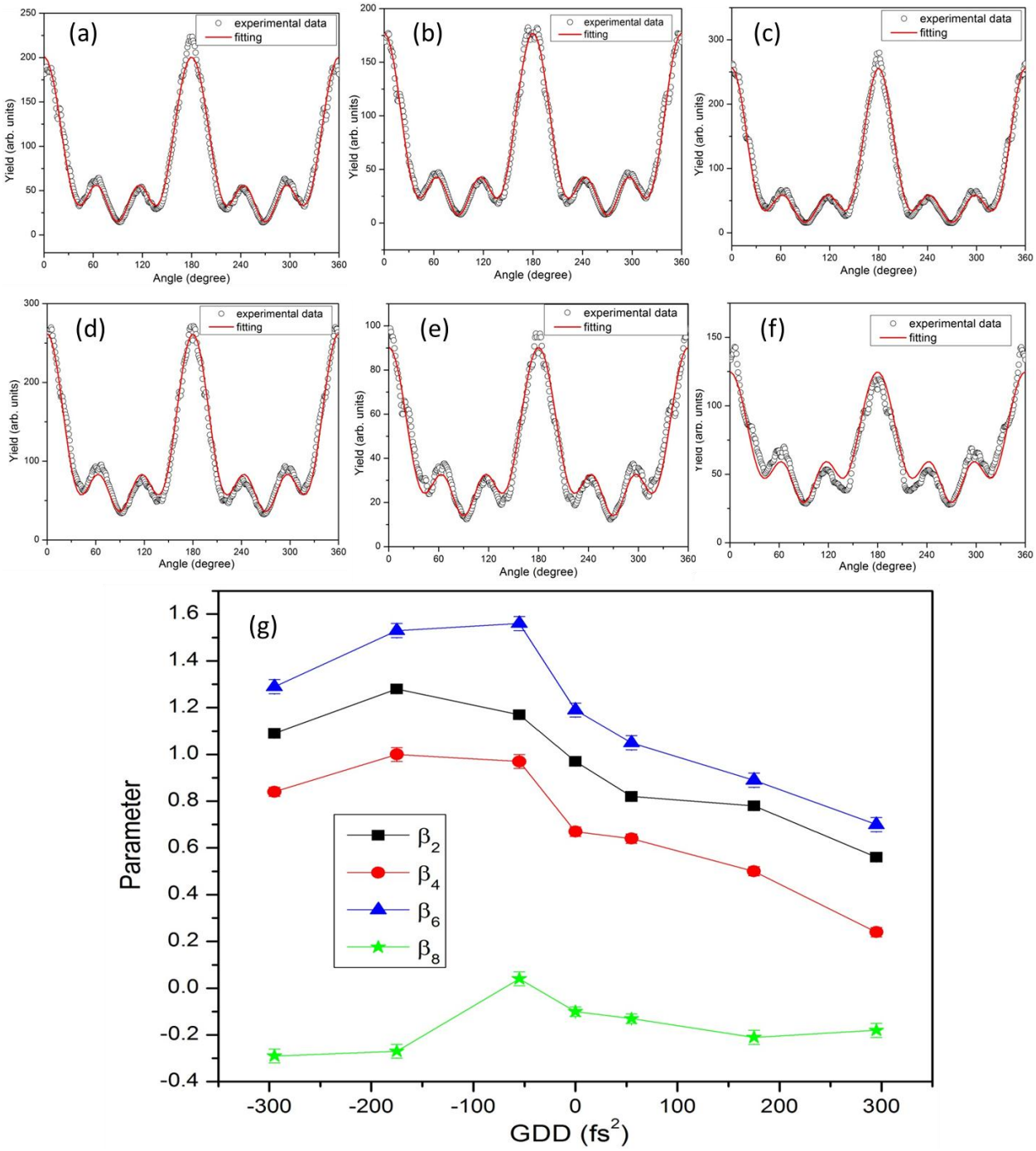

Figure 4.16 (a-f) PADs and fitting curves for the electrons in the energy region between 0.1 eV and 0.2 eV under different chirp conditions. The black hollow circles are the experimental data; the red curves are the fitting results according to equation (4.1). (a) -295 fs^2; (b) -175 fs^2; (c) -55 fs^2; (d) +55 fs^2; (e) +175 fs^2; (f) +295 fs^2; (g) The corresponding fitting results for the parameters β_2, β_4, β_6 and β_8.

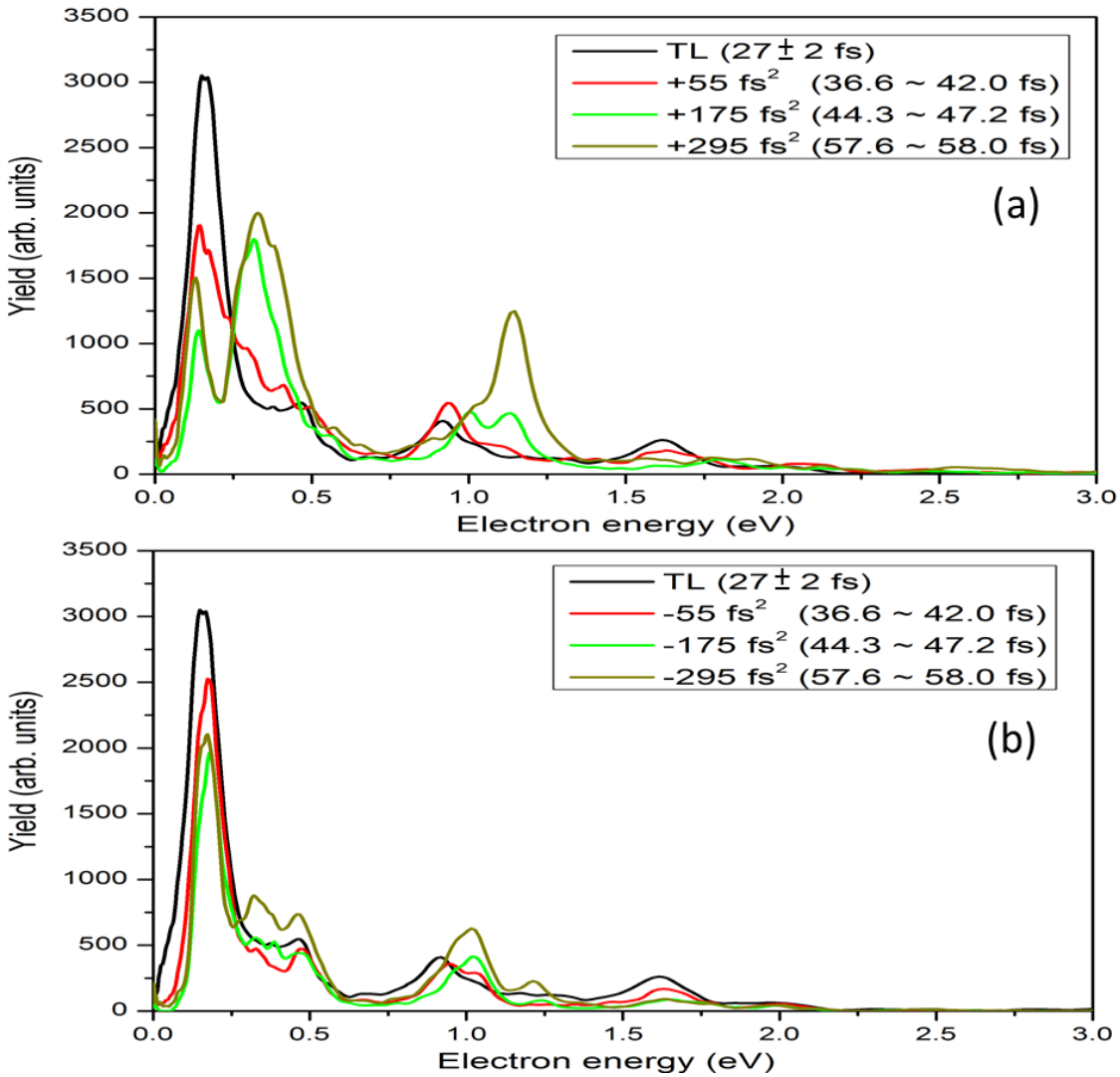

Figure 4.17 Photoelectron spectra for the FTL and chirped pulses at an intensity of 5.0×10^{12} W/cm^2. (a) Spectra for positively chirped pulses and the FTL pulse; (b) Spectra for negatively chirped pulses and the FTL pulse.

Earlier chirp dependent studies on C_{60} with longer pulse durations (with FTL pulses of more than 100 fs) showed only red or blue shifts of the photoelectron spectra [78]. However, as evident from our data, when a 27 fs FTL pulse is chirped, the spectra change with chirp. The pulse that we use has a broad bandwidth (over 100 meV) and it thus contains more wavelength components than the pulses with longer durations. Although the interpretation is tentative at this point without detailed theory, the broadband chirped pulses might ionize C_{60} through intermediate population of the "doorway" levels as shown in Fig. 4.2 [78]. In neutral C_{60},

excitation can occur from the HOMO to the LUMO+1 (t_{1g}). Relaxation to the LUMO may take place due to vibronic coupling. For the chirped pulses, the earlier arrived wavelength component might excite the electron to the "doorway" states. Ionization occurs within the remainder of the pulse. Depending on the temporal evolution of the chirped pulse and potential ionization saturation effects (which we, however, consider to be small at the used intensity), the final kinetic energy of the electron will be different and depend on the relaxation to the LUMO. This provides a potential explanation for the rising of the peak in the photoelectron spectra near 0.3 eV and 1.2 eV. Following this argumentation, this peak arises from the ionization after population of the "doorway" states.

4.4 Conclusions

In this chapter, the ionization mechanisms for C_{60} are investigated for about 30 fs laser pulses in the near-infrared spectral region and 50 fs laser pulses in the UV spectral region using Fourier transform-limited and chirped pulses. The photoelectrons are measured by a VMI spectrometer, providing PADs.

For near-infrared ionization, the observed low energy electrons show a six-lobe angular distribution at low laser intensities. This result differs from what is reported in Ref. [1]. The PADs were fitted by even orders of Legendre polynomials up to the 8^{th} order. For higher energies, the peaks qualitatively agree with earlier experimental work, where they have been assigned to ionization from SAMOs [1]. The angular distributions, however, show additional structure not consistent with these earlier assignments. Further experimental and theoretical work is needed to clarify the origin of these differences. For UV ionization, we obtain similar results as reported in Ref. [1], where the photoemission was attributed to the ionization from SAMOs. Due to residual non-isotropic thermal electron emission, the fitting results of the β_2 parameter give a slightly smaller value than reported in Ref. [1].

In the chirp dependence study on C_{60}, we find that chirped pulses influence the photoelectron energy spectra as well as the PADs. The reason for this behavior is tentatively assigned to the large bandwidth of the pulses and the importance of "doorway" states in the photoemission of C_{60} [66, 78]. For future work, the pulses will be fully characterized using a

FROG. The intensity dependence of the ionization of C_{60} with the chirped pulses should be further investigated to rule out saturation effects.

Right now a suitable theory to calculate the dynamics of C_{60} in ultrafast and strong laser fields is missing. Such theory would be helpful to explain, why we obtain different PADs with 30 fs IR pulses compared to the data obtained in a 120 fs laser field [1]. It is possible that we populate different SAMOs by using shorter pulses or alternative, observe additional contributions from other processes. It was shown by Remacle and coworkers that SAMOs exhibit an about 1000-fold cross-section for ionization as compared to Rydberg states [84]. The SAMOs, however, are less likely to be directly populated by photoexcitation (due to a lower cross section for excitation from the HOMO). The population pathway has not been resolved yet, but it likely involves vibronic relaxation. Since the SAMOs have much higher ionization probabilities than other states, once they are populated, they will dominate the photoelectron spectrum. It is conceivable that this will furthermore depend on the intensity of the laser fields. Further theoretical work may provide explanations for our observations.

Chapter 5 - Outlook

Our studies of the photoionization of the diatomic molecules CO and NO in two-color fields provide some basic understanding of the orientation dependence of the photoionization. Interestingly, the results did not agree with all theoretical predictions. The orientation dependent ionization probabilities of these molecules open possibilities to control non-adiabatic field-free orientation of such heteronuclear molecules with intense femtosecond two-color laser fields [32, 85].

Studying the collective electron dynamics in fullerenes can help to better understand the relationship between the few-electron dynamics in small molecules and the collective dynamics of many electrons in larger nano-systems. The SAMOs are found to play an important role in the photoionization of gas phase C_{60} [1]. To explore the dynamics of the population of SAMOs in C_{60} and in other fullerenes, pump-probe experiments with few-femtosecond time resolution are beneficial. A beam of ultrashort UV pulses around 200 nm may be used as the pump. The evolution of the photoelectron images will provide information on the timescale of the population and decay of the SAMOs.

References

[1] J. O. Johansson, G. G. Henderson, F. Remacle, and E. E. B. Campbell. Angular-resolved Photoelectron Spectroscopy of Superatom Orbitals of Fullerenes. *Phys. Rev. Lett.* **108**, 173401 (2012).

[2] A. H. Zewail. Femtochemistry: Atomic-Scale Dynamics of the Chemical Bond. *J. Phys. Chem. A* **104**, 5660 (2000).

[3] T. Brabec and F. Krausz. Intense few-cycle laser fields: Frontiers of nonlinear optics. *Rev. Mod. Phys.* **72**, 545 (2000).

[4] M. Hentschel, R. Kienberger, C. Spielmann, G. A. Reider, N. Milosevic, T. Brabec, P. Corkum, U. Heinzmann, M. Drescher, and F. Krausz. Attosecond metrology. *Nature* **414**, 509 (2001).

[5] P. M. Paul, E. S. Toma, P. Breger, G. Mullot, F. Augé, Ph. Balcou, H. G. Muller, P. Agostini. Observation of a Train of Attosecond Pulses from High Harmonic Generation. *Science* **292**, 1689 (2001).

[6] M. F. Kling and M. J. J. Vrakking. Attosecond Electron Dynamics. *Annu. Rev. Phys. Chem.* **59**, 463 (2008).

[7] E. E. B. Campbell, K. Hoffmann, H. Rottke, and I. V. Hertel. Sequential ionization of C_{60} with femtosecond laser pulses. *J. Chem. Phys.* **114**, 1716 (2001).

[8] F. Fabre, G. Petite, P. Agostini, and M. Clement. Multiphoton above-threshold ionization of xenon at 0.53 and 1.06 μm. *J. Phys. B: At. Mol. Phys.* **15**, 1353 (1982).

[9] J. H. Posthumus. The dynamics of small molecules in intense laser fields. *Rep. Prog. Phys*. **67**, 623 (2004).

[10] A. Scrinzi, M. Geissler, and T. Brabec. Ionization Above the Coulomb Barrier. *Phys. Rev. Lett*. **83**, 706 (1999).

[11] B. H. Bransden and C. J. Joachain. Physics of Atoms and Molecules. 2nd edition.

[12] G. Petite, F. Fabre, P. Agostini, M. Crance, and M. Aymar. Nonresonant multiphoton ionization of cesium in strong fields: Angular distributions and above-threshold ionization. *Phys. Rev. A* **29**, 2677 (1984).

[13] L. Zandee and R. B. Bernstein. Resonance-enhanced multiphoton ionization and fragmentation of molecular beams: NO, I_2, benzene, and butadiene. *J. Chem. Phys*. **71**, 1359 (1979).
[14] S. M. Park, S. Lu, and R. J. Gordon. Coherent laser control of resonance-enhanced multiphoton ionization of HCl. *J. Chem. Phys*. **94**, 8622 (1991).
[15] R. R. Freeman, P. H. Buckbaum, H. Milchberg, S. Darack, D. Schumacher, and M. E. Geusic. Above-Threshold Ionization with Subpicosecond Laser Pulses. *Phys. Rev. Lett.* **59**, 1092 (1987).
[16] J. H. Eberly, J. Javanainen, and K. Rzazewski. Above-threshold ionization. *Phys. Rep.* **204**, 331 (1991).
[17] G. G. Paulus, W. Nicklich, H. Xu, P. Lambropoulos, and H. Walther. Plateau in Above Threshold Ionization Spectra. *Phys. Rev. Lett*. **72**, 2851 (1994).
[18] L. V. Keldysh. Ionization in the Field of a Strong Electromagnetic Wave. *Sov. Phys. JETP* **20**, 1307 (1965).
[19] P. B. Corkum. Plasma Perspective on Strong-Field Multiphoton Ionization. *Phys. Rev. Lett*. **71**, 1994 (1993).
[20] K. J. Schafer, B. Yang, L. F. DiMauro, and K. C. Kulander. Above Threshold Ionization Beyond the High Harmonic Cutoff. *Phys. Rev. Lett.* **70**, 1599 (1993).
[21] N. J. Kylstra, A. M. Ermdaev, C. J. Joachain. Relativistic effects in the time evolution of a one-dimensional model atom in an intense laser field. *J. Phys. B: At. Mol. Opt. Phys.* **30**, L449 (1997).
[22] E. E. B. Campbell, K. Hoffmann, H. Rottke, and I. V. Hertel. Sequential ionization of C_{60} with femtosecond laser pulses. *J. Chem. Phys.* **114**, 1716 (2001).
[23] E. E. B. Campbell, K. Hansen, K. Hoffmann, G. Korn, M. Tchaplyguine, M. Wittmann, and I. V. Hertel. From Above Threshold Ionization to Statistical Electron Emission: The Laser Pulse-Duration Dependence of C_{60} Photoelectron Spectra. *Phys. Rev. Lett*. **84**, 2128 (2000).
[24] M. Kjellberg, O. Johansson, F. Jonsson, A. V. Bulgakov, C. Bordas, E. E. B. Campbell, and K. Hansen. Momentum-map-imaging photoelectron spectroscopy of fullerenes with femtosecond laser pulses. *Phys. Rev. A* **81**, 023202 (2010).

[25] A. T. J. B. Eppink and D. H. Parker. Velocity map imaging of ions and electrons using electrostatic lenses: Application in photoelectron and photofragment ion imaging of molecular oxygen. *Rev. Sci. Instrum.* **68**, 3477 (1997).
[26] C. Bordas, F. Paulig, H. Helm, and D. L. Huestis. Photoelectron imaging spectrometry: Principle and inversion method. *Rev. Sci. Instrum.* **67**, 2257 (1996).
[27] M. J. J. Vrakking. An iterative procedure for the inversion of two-dimensional ion/photoelectron imaging experiments. *Rev. Sci. Instrum.* **72**, 4084 (2001).
[28] K. L. Reid. Photoelectron Angular Distributions. *Annu. Rev. Phys. Chem.* **54**, 397 (2003).
[29] P. Maine, D. Strickland, P. Bado, M. Pessot, and G. Mourou. Generation of Ultrahigh Peak Power Pulses by Chirped Pulse Amplification. *IEEE J. Quant. Electron.* **24**, 398 (1988).
[30] F. Süßmann, S. Zherebtsov, J. Plenge, N. G. Johnson, M. Kübel, A. M. Sayler, V. Mondes, G. Graf, E. Rühl. G. G. Paulus, D. Schmischke, P. Swrschek, and M. F. Kling. Single-shot velocity-map imaging of attosecond light-field control at kilohertz rate. *Rev. Sci. Instrum*. **82**, 093109 (2011).
[31] B. Sheehy, B. Walker, and L. F. Dimauro. Phase Control in the Two-Color Photodissociation of HD^+. *Phys. Rev. Lett*. **74**, 4799 (1995).
[32] S. De, I. Znakovskaya, D. Ray, F. Anis, N. G. Johnson, I. A. Bocharova, M. Magrakvelidze, B. D. Esry, C. L. Cocke, I. V. Litvinyuk, and M. F. Kling. Field-Free Orientation of CO Molecules by Femtosecond Two-Color Laser Fields. *Phys. Rev. Lett*. **103**, 153002 (2009).
[33] D. Ray, Z. Chen, S. De, W. Cao, I. V. Litvinyuk, A. T. Le, C. D. Lin, M. F. Kling, and C. L. Cocke. Momentum spectra of electrons rescattered from rare-gas targets following their extraction by one- and two-color femtosecond laser pulses. *Phys. Rev. A* **83**, 013410 (2011).
[34] M. Magrakvelidze, F. He, S. De, I. Bocharova, D. Ray, U. Thumm, and I. V. Litvinyuk. Angular dependence of the strong-field ionization measured in randomly oriented hydrogen molecules. *Phys. Rev. A* **79**, 033408 (2009).
[35] I. Znakovskaya, P. von den Hoff, S. Zherebtsov, A. Wirth, O. Herrwerth, M. J. J. Vrakking, R. de Vivie-Riedle, and M. F. Kling. Attosecond Control of Electron Dynamics in Carbon Monoxide. *Phys. Rev. Lett*. **103**, 103002 (2009).
[36] J. Abrefah, D. R. Olander, M. Balooch, and W. J. Siekhaus. Vapor Pressure of Buckminsterfullerene. *Appl. Phys. Lett*. **60**, 1313 (1992).

[37] H. Li, D. Ray, S. De, I. Znakovskaya, W. Cao, G. Laurent, Z. Wang, M. F. Kling, A. T. Le, and C. L. Cocke. Orientation dependence of the ionization of CO and NO in an intense femtosecond two-color laser field. *Phys. Rev. A* **84**, 043429 (2011).
[38] F. H. M. Faisal. Multiple absorption of laser photons by atoms. *J. Phys. B: At. Mol. Phys.* **6**, L89, (1973).
[39] H. R. Reiss. Effect of an intense electromagnetic field on a weakly bound system. *Phys. Rev. A* **22**, 1786 (1980).
[40] X. M. Tong, Z. X. Zhao, and C. D. Lin. Theory of molecular tunneling ionization. *Phys. Rev. A* **66**, 033402 (2002).
[41] A. S. Alnaser, S. Voss, X. M. Tong, C. M. Maharjan, P. Ranitovic, B. Ulrich, T. Osipov, B. Shan, Z. Chang, and C. L. Cocke. Effects of Molecular Structure on Ion Disintegration Patterns in Ionization of O_2 and N_2 by Short Laser Pulses. *Phys. Rev. Lett.* **93**, 113003 (2004).
[42] P. von den Hoff, I. Znakovskaya, S. Zherebtsov, M. F. Kling, and R. de Vivie-Riedle. Effects of multi orbital contributions in the angular-dependent ionization of molecules in intense few-cycle laser pulses. *Phys. B* **98**, 659 (2010).
[43] A. Staudte, S. Patchkovskii, D. Pavičić, H. Akagi, O. Smimova, D. Zeidler, M. Meckel, D. M. Villeneuve, R. Dörner, M. Yu. Ivanov, and P. B. Corkum. Angular Tunneling Ionization Probability of Fixed-in-Space H_2 Molecules in Intense Laser Pulses. *Phys. Rev. Lett*. **102**, 033004 (2009).
[44] H. Akagi, T. Otobe, A. Staudte, A. Shiner, F. Turner, R. Dörner, D. M. Villeneuve, and P. B. Corkum. Laser Tunnel Ionization from Multiple Orbitals in HCl. *Science* **325**, 1364 (2009).
[45] L. Holmegaard, J. L. Hansen, L. Kalhøj, S. L. Kragh, H. Stapelfeldt, F. Filsinger, J. Küpper, G. Meijer, D. Dimitrovski, M. Abu-samha, C. P. J. Martiny, and L. B. Madsen. Photoelectron angular distributions from strong-field ionization of oriented molecules. *Nature Physics* **6**, 428 (2010).
[46] L. V. Litvinyuk, K. F. Lee, P. W. Dooley, D. M. Rayner, D. M. Villeneuve, and P. B. Corkum. Alignment-Dependent Strong Field Ionization of Molecules. *Phys. Rev. Lett.* **90**, 233003 (2003).
[47] D. Pavičić, K. F. Lee, D. M. Rayner, P. B. Corkum, and D. M. Villeneuve. Direct Measurement of the Angular Dependence of Ionization for N_2, O_2 and CO_2 in Intense Laser Fields. *Phys. Rev. Lett*. **98**, 243001 (2007).

[48] L. Holmegaard, J. H. Nielsen, I. Nevo, and H. Stapelfeldt. Laser-Induced Alignment and Orientation of Quantum-State-Selected Large Molecules. *Phys. Rev. Lett*. **102**, 023001 (2009).
[49] A. S. Alnaser, C. M. Maharjan, X. M. Tong, B. Ulrich, P. Ranitovic, B. Shan, Z. Chang, C. D. Lin, C. L. Cocke, and I. V. Litvinyuk. Effects of orbital symmetries in dissociative ionization of molecules by few-cycle laser pulses. *Phys. Rev. A* **71**, 031403(R) (2005).
[50] S. Voss, A. S. Alnaser, X. M. Tong, C. Maharjan, P. Ranitovic, B. Ulrich, B. Shan, Z. Chang, C. D. Lin, and C. L. Cocke. High resolution kinetic energy release spectra and angular distributions from double ionization of nitrogen and oxygen by short laser pulses. *J. Phys. B: At. Mol. Opt. Phys.* **37**, 4239 (2004).
[51] I. Znakovskaya, P. von den Hoff, N. Schirmel, G. Urbasch, S. Zherebtsov, B. Bergues, R. de Vivie-Riedle, K.-M. Weitzel, and M. F. Kling. Waveform control of orientation-dependent ionization of DCl in few-cycle laser fields. *Phys. Chem. Chem. Phys.* **13**, 8653 (2011).
[52] D. Dimitrovski, C. P. J. Martiny, and L. B. Madsen. Strong-field ionization of polar molecules: Stark-shift-corrected strong-field approximation. *Phys. Rev. A* **82**, 053404 (2010).
[53] M. Abu-samha and L. B. Madsen. Photoelectron angular distributions from polar molecules probed by intense femtosecond lasers. *Phys. Rev. A* **82**, 043413 (2010).
[54] A. Etches and L. B. Madsen. Extending the strong-field approximation of high-order harmonic generation to polar molecules: gating mechanisms and extension of the harmonic cutoff. *J. Phys. B: At. Mol. Opt. Phys.* **43**, 155602 (2010).
[55] Z. Chen, A. T. Le, T. Morishita, and C. D. Lin. Quantitative rescattering theory for laser-induced high-energy plateau photoelectron spectra. *Phys. Rev. A* **79**, 033409 (2009).
[56] T. Morishita, A. T. Le, Z. Chen, and C. D. Lin. Accurate Retrieval of Structural Information from Laser-Induced Photoelectron and High-Order Harmonic Spectra by Few-Cycle Laser Pulses. *Phys. Rev. Lett.* **100**, 013903 (2008).
[57] P. von den Hoff, I. Znakovskaya, M. F. Kling, and R. de Vivie-Riedle. Attosecond control of the dissociative ionization via electron localization: A comparison between D_2 and CO. *Chem. Phys.* **366**, 139 (2009).
[58] M. Lundqvist, P. Baltzer, D. Edvardsson, L. Karlsson, and B. Wannberg. Novel Time of Flight Instrument for Doppler Free Kinetic Energy Release Spectroscopy. *Phys. Rev. Lett*. **75**, 1058 (1995).

[59] S. De, M. Magrakvelidze, I. A. Bocharova, D. Ray, W. Cao, I. Znakovskaya, H. Li, Z. Wang, G. Laurent, U. Thumm, M. F. Kling, I. V. Litvinyuk, I. Ben-Itzhak, and C. L. Cocke. Following dynamic nuclear wave packets in N_2, O_2, and CO with few-cycle infrared pulses. *Phys. Rev. A* **84**, 043410 (2011).

[60] A. Zavriyev, P. H. Bucksbaum, H. G. Muller, and D. W. Schumacher. Ionization and dissociation of H_2 in intense laser fields at 1.064 μm, 532 nm, and 355 nm. *Phys. Rev. A* **42**, 5500 (1990).

[61] J. Muth-Böhm, A. Becker, and F. H. M. Faisal. Suppressed Moleculear Ionization for a Class of Diatomics in Intense Femtosecond Laser Fields. *Phys. Rev. Lett.* **85**, 2280 (2000).

[62] J. L. Hansen and H. Stapelfeldt. Time-Resolved Photoelectron Angular Distributions from Strong-Field Ionization of Rotating Naphthalene Molecules. *Phys. Rev. Lett*. **106**, 073001 (2011).

[63] M. J. Frisch *et al*., compute code GAUSSIAN 03, revision C. 02, Gaussian, Inc., Pittsburgh, PA, 2003.

[64] P. H. Bucksbaum, A. Zavriyev, H. G. Muller, and D. W. Schumacher. Softening of the H_2^+ Molecular Bond in Intense Laser Fields. *Phys. Rev. Lett*. **64**, 1883 (1990).

[65] M. Feng, J. Zhao and H. Petek. Atomlike, Hollow-Core-Bound Molecular Orbitals of C_{60}. *Science* **320**, 359 (2008).

[66] M. Boyle, M. Hedén, C. P. Schulz, E. E. B. Campbell, and I. V. Hertel. Two-color pump-probe study and internal-energy dependence of Rydberg-state excitation in C_{60}. *Phys. Rev. A* **70**, 051201 (R) (2004).

[67] Wikipedia: buckminsterfullerene.

[68] E. Osawa, Kagaku, *Chem. Abstr*. **74**, 75698v (1971).

[69] H. W. Kroto, J. R. Heath, S. C. O'Brien, R. F. Curl, and R. E. Smalley. C_{60}: Buckminsterfullerene. *Nature* **318**, 162 (1985).

[70] H. Hohmann, C. Callegari, S. Furrer, D. Grosenick, E. E. B. Campbell, and I. V. Hertel. Photoionization and Fragmentation Dynamics of C_{60}. *Phys. Rev. Lett.* **73**, 1919 (1994).

[71] S. Hunsche, T. Starczewski, A. l'Huillier, A. Persson, C.-G. Wahlström, B. van Linden van den Heuvell, and S. Svanberg. Ionization and Fragmentation of C_{60} via Multiphoton-Multiplasmon Excitation. *Phys. Rev. Lett.* **77**, 1966 (1996).

[72] G. von Helden, I. Holleman, G. M. H. Knippels, A. F. G. van der Meer, and G. Meijer. Infrared Resonance Enhanced Multiphoton Ionization of Fullerenes. *Phys. Rev. Lett*. **79**, 5234 (1997).
[73] E. E. B. Campbell, K. Hoffmann, H. Rottke, and I. V. Hertel. Sequential ionization of C_{60} with femtosecond laser pulses. *J. Chem. Phys.* **114**, 1716 (2001).
[74] E. E. B. Campbell and K. Hansen, K. Hoffmann, G. Korn, M. Tchaplyguine, M. Wittmann, and I. V. Hertel. From Above Threshold Ionization to Statistical Electron Emission: The Laser Pulse-Duration Dependence of C_{60} Photoelectron Spectra. *Phys. Rev. Lett*. **84**, 2128 (2000).
[75] M. Tchaplyguine, K. Hoffmann, O. Dühr, H. Hohmann, G. Korn, H. Rottke, M. Wittmann, I. V. Hertel, and E. E. B. Campbell. Ionization and fragmentation of C_{60} with sub-50 fs laser pulses. *J. Chem. Phys*. **112**, 2781 (2000).
[76] E. E. B. Campbell, G. Ulmer, and I. V. Hertel. Delayed Ionization of C_{60} and C_{70}. *Phys. Rev. Lett.* **67**, 1986 (1991).
[77] M. Boyle, K. Hoffmann, C. P. Schulz, I. V. Hertel, R. D. Levine, and E. E. B. Campbell. Excitation of Rydberg Series in C_{60}. *Phys. Rev. Lett*. **87**, 273401 (2001).
[78] M. Boyle, T. Laarmann, K. Hoffmann, M. Hedén, E. E. B. Campbell, C. P. Schulz, and I. V. Hertel. Excitation dynamics of Rydberg states in C_{60}. *Eur. Phys. J. D* **36**, 339 (2005).
[79] I. Shchatsinin, T. Laarmann, N. Zhavoronkov, C. P. Schulz, and I. V. Hertel. Ultrafast energy redistribution in C_{60} fullerenes: A real time study by two-color femtosecond spectroscopy. *J. Chem. Phys.* **129**, 204308 (2008).
[80] M. Kjellberg, J. O. Johansson, F. Jonsson, A. V. Bulgakov, C. Bordas, E. E. B. Campbell, and K. Hansen. Momentum-map-imaging photoelectron spectroscopy of fullerenes with femtosecond laser pulses. *Phys. Rev. A* **81**, 023202 (2010).
[81] J. O. Johansson, J. Fedor, M. Goto, M. Kjellberg, J. Stenfalk, G. G. Henderson, E. E. B. Campbell, and K. Hansen. Anisotropic hot electron emission from fullerenes. *J. Chem. Phys.* **136**, 164301 (2012).
[82] S. T. Manson and A. F. Starace. Photoelectron angular distributions: energy dependence for s subshells. *Rev. Mod. Phys.* **54**, 389 (1982).
[83] D.L. Lichtenberger, K. W. Nebesny, C.D. Ray, D. R. Hoffman, and L. D. Lamb. Valence and core photoelectron spectroscopy of C_{60}, buckminsterfullerene. *Chem. Phys. Lett.* **176**, 203 (1991).

[84] B. Mignolet, J. O. Johansson, E. E. B. Campbell, and F. Remacle. Probing Rapidly Ionizing Super-Atom Molecular Orbitals in Fullerenes: A computational and fs Photoelectron Spectroscopy Study. submitted.
[85] M. Spanner, S. Patchkovskii, E. Frumker, and P. Corkum. Mechanisms of Two-color Laser-Induced Field-Free Molecular Orientation. *Phys. Rev. Lett*. **109**, 113001 (2012).
[86] D. N. Fittinghoff, P. R. Bolton, B. Chang, and K. C. Kulander. Observation of Nonsequential Double Ionization of Helium with Optical Tunneling. *Phys. Rev. Lett*. **69**, 2642 (1992).
[87] B. Walker, E. Mevel, B. Yang, P. Breger, J. P. Chambaret, A. Antonetti, L. F. Dimauro, and P. Agostini. Double ionization in the perturbative and tunneling regimes. *Phys. Rev. A* **48**, R894 (1993).
[88] B. Shan, C. Wang, and Z. Chang. High peak-power kilohertz laser system employing single-stage multi-pass amplification. U. S. Patent No. 7050474, issued May 23, 2006.
[89] R. Trebino and D. J. Kane. Using phase retrieval to measure the intensity and phase of ultrafast pulses: frequency-resolved optical gating. *J. Opt. Soc. Am. A* **10**, 1101 (1993).
[90] J. O. Johansson and E. E. B. Campbell. Probing excited electronic states and ionization mechenisms of fullerenes. Chem. Soc. Rev. Tutorial review (2013).
[91] C. M. Maharjan, A. S. Alnaser, I. Litvinyuk, P. Ranitovic, and C. L. Cocke. Wavelength dependence of momentum-space images of low-energy electrons generated by short intense laser pulses at high intensities. *J. Phys. B: At. Mol. Opt. Phys*. **39**, 1955 (2006).